Meccanica (2020) 55:1561–1584
https://doi.org/10.1007/s11012-020-01194-2

# Controlling the natural convection flow through a flexible baffle in an L-shaped enclosure

**Mohammad Ghalambaz · S. A. M. Mehryan · Ammar I. Alsabery · Ahmad Hajjar · Mohesn Izadi · Ali Chamkha**

Received: 4 November 2019 / Accepted: 9 June 2020

**Abstract** The free convection flow through a flexible baffle in an L-shaped enclosure has been numerically analyzed. The governing equations are introduced in an Arbitrary Lagrangian–Eulerian moving mesh frame. The full governing equations respect to boundary conditions were solved numerically using FEM. A grid-independent test was performed to ensure the accuracy of the results, and the results of the numerical solver are compared with previous works. The influence of the dimensionless parameters, including Rayleigh number, the elasticity modulus and the length of the flexible baffle investigated on the flow and heat transfer. Results indicate that a stiffer baffle tends to resist the fluid flow and inhibits convective heat transfer. For a higher value of Ra, a larger baffle results in more resistance to the flow and inhibits heat transfer, while, at the same time, increases the stress over the baffle.

**Keywords** Natural convection heat transfer · Flexible-baffle · Arbitrary Lagrangian–Eulerian (ALE)

M. Ghalambaz
Metamaterials for Mechanical, Biomechanical and Multiphysical Applications Research Group, Ton Duc Thang University, Ho Chi Minh City, Vietnam
e-mail: mohammad.ghalambaz@tdtu.edu.vn

M. Ghalambaz
Faculty of Applied Sciences, Ton Duc Thang University, Ho Chi Minh City, Vietnam

S. A. M. Mehryan
Young Researchers and Elite Club, Yasooj Branch, Islamic Azad University, Yasooj, Iran

A. I. Alsabery
Refrigeration & Air-conditioning Technical Engineering Department, College of Technical Engineering, The Islamic University, Najaf, Iraq

A. I. Alsabery
Department of Mathematical Sciences, Faculty of Science & Technology, Universiti Kebangsaan Malaysia (UKM), 43600 Bangi, Selangor, Malaysia

A. Hajjar
LabECAM, ECAM Lyon, Université de Lyon, Lyon, France

M. Izadi
Mechanical Engineering Department, Faculty of Engineering, Lorestan University, Khorramabad, Iran

A. Chamkha (✉)
Institute of Research and Development, Duy Tan University, Da Nang 550000, Vietnam
e-mail: alichamkha@duytan.edu.vn

A. Chamkha
Institute of Theoretical and Applied Research (ITAR), Duy Tan University, Hanoi 100000, Vietnam

## List of symbols

| | |
|---|---|
| $\boldsymbol{g}$ | Gravity-constant vector |
| $L$ | Height of the cavity |
| $W$ | Width of the cavity |
| $B$ | Length of the flexible baffle |
| $E$ | Young's modulus in dimensional form |
| $\boldsymbol{d}_s$ | Vector of displacement |
| $f$ | Frequency |
| $\boldsymbol{F}_v$ | Vector of body force |
| $E_\tau$ | Non-dimensional form of the elasticity modulus |
| $Pr$ | Prandtl number |
| $P$ | Fluid pressure |
| $k$ | Thermal conductivity |
| $t$ | Dimensional time |
| $Ra$ | Thermal Rayleigh number |
| $\boldsymbol{w}$ | The vector of velocity for the mesh motion |
| $T$ | Temperature |
| $\boldsymbol{u}$ | Velocity in a vector form |
| $y$ | Cartesian coordinate in $y$ direction |
| $x$ | Cartesian coordinate in $x$ direction |

## Greek symbols

| | |
|---|---|
| $\rho$ | Density |
| $v$ | Poisson's ratio |
| $\sigma$ | Stress tensor, von Mises stress |
| $\tau$ | Non-dimensional time |
| $\rho_R$ | The ratio of the fluid's density to the structure's density |
| $\beta$ | Volumetric thermal expansion coefficient |
| $\mu$ | Dynamic viscosity |
| $\alpha$ | Thermal diffusivity |

## Subscripts

| | |
|---|---|
| $h$ | Hot temperature |
| $av$ | Average |
| $s$ | Flexible baffle |
| $f$ | Fluid |
| $c$ | Cold temperature |
| $p$ | Membrane partition |

## Superscripts

| | |
|---|---|
| * | The parameters in a dimensional form |

## 1 Introduction

Passive enhancement of heat transfer is one of the effective ways to improve the performance of thermal equipment, while not significantly increasing the power consumption of these devices. The concept of Fluid–structure interaction is one of the new ideas pursuing such a goal. The vibration of electronic devices derived by cooling fan, sterling and mixing devices, and shake of heat exchangers elements stand within the scope of FSI problems. Such issues arise when fluid and solid interactions occur at the joint boundary.

The impact of an oscillating fin on the heat transfer and fluid flow inside a lid-driven cavity was investigated by Shi and Khodadadi [1, 2]. Jamesahar et al. [3] studied natural convection heat transfer inside a divided enclosure using a flexible membrane. They inquired about the influence of membrane deformation on heat transfer. Features of turbulent flows derived by the oscillation of elastic structures were studied by Gomes and Lienhart [4]. Al-Amiri and Khanafer [5] studied mixed convection heat transfer inside an enclosure with an elastic wall. The fluid and structure domains are fully coupled. They reported that the flexibility of the bottom wall results in heat transfer enhancement. In addition, the contribution of forced to natural convection heat transfer has a major impact on the elastic wall, movement, and energy transfer through the enclosure. Soti et al. [6] investigated an increment of heat transfer using a large-scale flow derived by deflection of a thin elastic structure.

The unsteady mixed convection of an assembled enclosure-channel induced by the interaction of flexible walls and fluid flow is numerically analyzed by Sabbar et al. [7]. In contrast with rigid walls, the flexible wall(s) enhances the heat transfer rate by about 17%. Joshi et al. [8] examined the laminar forced convection flow and heat transfer in a channel in the presence of a set of flexible plates. The plates were flexible and perpendicular to the fluid flow. The plates bend due to the fluid interaction, which affects the flow and heat transfer in the channel. The bending of the plates reduced the thickness of the thermal boundary layer and improved the heat transfer at the channel walls. Park et al. [9] utilized the immersed boundary method and explored the mixed convection flow and heat transfer over a flexible cylinder in a channel. They interestingly found that the cylinder could be at two states of stretched-stable or flapping states due to fluid–structure interaction with the flow. The self-sustained flapping state of the flexible cylinder could provide a better heat transfer performance compared to that of the stretched-stable state.

Considering an elastic fin, natural convection heat transfer of an FSI problem inside the cavity was studied by Alsabery et al. [10]. A meaningful effect of the flexible fin on natural convection and the fluid flow was reported. In another study, Alsabery et al. [11] characterized transient mixed convection and entropy generation inside the enclosure with an elastic wall. The case of lower values of the elastic wall obliquity and counter-clockwise spin of the circular cylinder showed the highest global entropy generation and also natural convection. Mehryan et al. [12] studied the natural convection inside a tilted divided enclosure by an elastic membrane.

Natural heat transfer through an enclosure is a well-known problem in industrial and power engineering equipment such as microelectronic chips, photovoltaic sheets, and cooling electronic devices. Conventional methods of investigating heat transfer inside enclosures have attracted the attention of many researchers such as Chamkha et al. [13, 14], Tayebi and Chamkha [15], Kumar et al. [16], Dogonchi et al. [17], and Alsabery et al. [18] considered the natural convection inside cavities exposed to magnetic fields. The enclosures have also been used containers for cooling of domestic radiators [19], thermal energy storage [20–22], welling space air heating [23, 24], and electronic cooling [25].

The geometry parameter is a significant control index for heat transfer related to thermal systems [26–32]. Investigating and studying the natural convection heat transfer inside different geometries such as T-shaped [28, 33], L-shaped [34, 35], U-shaped [36, 37], C-shape [38] have been the subject of much research. These researches have been looking for ways to increase heat transfer using optimum geometry.

As mentioned above, one of the ways to increase and control free convection heat transfer is to use flexible structures in cooling. In this study, the effect of a flexible fin, which acts in the form of a baffle, is addressed on convective heat transfer in an L-shaped cavity.

## 2 Mathematical model and formulation

As illustrated in Fig. 1, an L-shaped enclosure having the height and width of $L^*$ and $D^*$, respectively, is considered as the problem of the current study. It is worth noting that $L^*$ is equal to $D^*$ and is the length scale. A flexible baffle having the length of $l_b^*$ is connected to the vertical cold wall. In addition to the right vertical wall, a horizontal wall, which can be seen in Fig. 1, is also kept in the cold temperature of $T_c^*$. The left vertical and bottom horizontal walls of the enclosure are at a high temperature of $T_h^*$. The flexible baffle of thickness $t_b^*$ is considered to be isotropic and uniform. The Newtonian fluid, flowing inside the cavity, is incompressible and laminar. The flexible baffle weight and the buoyancy force are two body forces exerted to the flexible baffle, and the surface of the baffle is also exposed to normal and tangential tensions due to the hydrodynamic forces.

According to the mentioned assumptions, a numerical model is developed to study the hydrodynamic and thermal performances of a Newtonian fluid in the computational domain of the L-shaped cavity, including a flexible baffle. The formulated equations in the Arbitrary Lagrangian–Eulerian (ALE) coordinate system introduced as [12, 39]:

*Mass conservation*:

$$\nabla^* \cdot \boldsymbol{u}^* = 0 \tag{1}$$

*Momentum conservation*:

$$\rho_f^* \left[ \frac{\partial \boldsymbol{u}^*}{\partial \tau^*} + (\boldsymbol{u}^* - \boldsymbol{w}^*) \cdot \nabla^* \boldsymbol{u}^* \right] + \nabla^* P^* - \mu_f^* \nabla^{*^2} \boldsymbol{u}^* - \rho_f^* g^* \beta_f^* (T^* - T_c^*) \boldsymbol{j} = 0 \tag{2}$$

*Energy conservation for the fluid*:

$$\rho_f^* C_{p,f}^* \left[ \frac{\partial T^*}{\partial \tau^*} + (\boldsymbol{u}^* - \boldsymbol{w}^*) \cdot \nabla^* T^* \right] - k_f^* \nabla^{*^2} T^* = 0 \tag{3}$$

*Energy conservation for the flexible baffle*:

$$\frac{\partial T^*}{\partial \tau^*} - k_s^* \nabla^{*^2} T^* = 0 \tag{4}$$

where the mesh and the fluid velocities are indicated by $\boldsymbol{w}^*$ and $\boldsymbol{u}^*$, respectively. Here $P^*$ and $T^*$ are the pressure and temperature. The density and thermal diffusivity are represented using $\rho^*$ and $\alpha^*$, respectively, and the subscripts $s$ and $f$ represent the solid and fluid properties.

*Structural displacement of the flexible baffle*:

$$\rho_s^* \frac{d^2\boldsymbol{d}_s^*}{d\tau^{*2}} - \nabla^*\boldsymbol{\sigma}^* - \boldsymbol{F}_v^* = 0 \tag{5}$$

where $\boldsymbol{d}_s^*$ the flexible baffle displacement vector, $\boldsymbol{F}_v^*$ the body force imposed on the flexible baffle. Also, $\sigma^*$ is the stress tensor and can be defined as:

$$\boldsymbol{\sigma}^* = {J^*}^{-1} F^* S^* {F^*}^{tr},\ F^* = \left(I + \nabla^*\boldsymbol{d}_s^*\right) \& J^* = det(F^*) \tag{6}$$

$S^*$ is the second-order Piola–Kirchhoff stress can be related to the strain, i.e. $\varepsilon$, by the following relation:

$$\begin{aligned}
S^* &= \partial Z_s^* / \partial \varepsilon^* \\
Z_s^* &= \frac{1}{2}\mu_l^*\left(J^{*-1}I_1 - 3\right) - \mu_l^* \ln(J^*) + \frac{1}{2}\lambda^*(\ln(J^*))^2 \\
\varepsilon^* &= \frac{1}{2}\left(\nabla^*\boldsymbol{d}_s^* + \nabla^*\boldsymbol{d}_s^{*tr} + \nabla^*\boldsymbol{d}_s^{*tr}\nabla^*\boldsymbol{d}_s^*\right) \\
\mu_l^* &= E_\tau^*/2(1+v^*) \\
\lambda^* &= E_\tau^* v^*/[(1+v^*)(1-2v^*)]
\end{aligned} \tag{7}$$

In the above, $E_\tau^*$ and $v^*$ are the Young's modulus and Poisson's ratio. To better describe the flow field, stream function, $\psi^*$, is employed:

$$\nabla^{*^2}\psi^* + \nabla^* \times \boldsymbol{u}^* = 0 \tag{8}$$

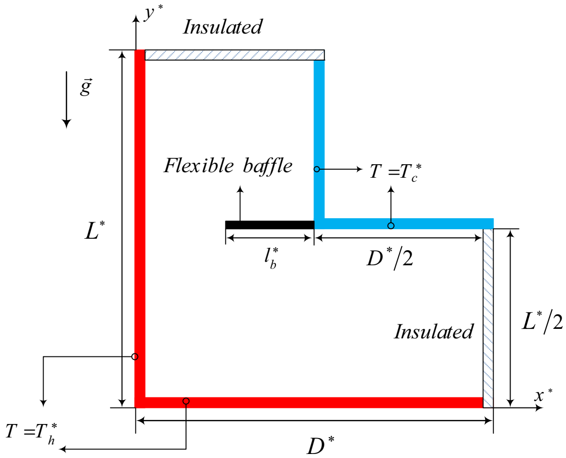

**Fig. 1** A schematic diagram of the physical model for the L-shaped cavity with a flexible baffle

$\nabla^*$ in the above equation is:

$$\nabla^* = \frac{\partial}{\partial x^*}\boldsymbol{i} + \frac{\partial}{\partial y^*}\boldsymbol{j} \tag{9}$$

which $\boldsymbol{i}$ and $\boldsymbol{j}$ are the unit vectors along the $x^*$ and $y^*$ axes. Taking into account the no-slip boundary condition at the solid surfaces, the boundary conditions in the dimensional coordinates are as below:

$$\forall x^*, y^* \left| \begin{array}{l} y^* = 0, 0 \le x^* \le L^* \\ x^* = 0, 0 \le y^* \le L^* \end{array} \right. \Rightarrow T^* = T_h^*,\ u^* = v^* = 0 \tag{10-a}$$

$$\forall x^*, y^* \left| \begin{array}{l} x^* = L^*/2,\ L^*/2 \le y^* \le L^* \\ y^* = L^*/2,\ L^*/2 \le x^* \le L^* \end{array} \right. \Rightarrow T^* = T_c^*,\ u^* = v^* = 0 \tag{10-b}$$

$$\forall x^*, y^*\ |x^* = L^*,\ 0 \le y^* \le L^*/2 \Rightarrow \frac{\partial T^*}{\partial x^*} = 0,\quad u^* = v^* = 0 \tag{10-c}$$

$$\forall x^*, y^*\ |y^* = L^*,\ 0 \le x^* \le L^*/2 \Rightarrow \frac{\partial T^*}{\partial y^*} = 0,\quad u^* = v^* = 0 \tag{10-d}$$

Also, at the interface of the fluid and flexible baffle:

$$k_f^*\left(\frac{\partial T^*}{\partial n}\right)_f = k_s^*\left(\frac{\partial T^*}{\partial n}\right)_s,\ \frac{\partial \boldsymbol{d}_s^*}{\partial \tau^*} = \boldsymbol{u}^*, \boldsymbol{\sigma}^* \cdot n = -P^* + \mu_f^* \nabla^* \boldsymbol{u}^* \tag{10-e}$$

It is worth noting that $n$ of the above equations is the normal vector on the flexible baffle. Invoking the below non-dimensional parameters, the governing equations can be non-dimensionalized.

$$\begin{aligned}
&\boldsymbol{d}_s = \frac{\boldsymbol{d}_s^*}{L^*},\ \boldsymbol{\sigma} = \frac{\boldsymbol{\sigma}^*}{E_\tau^*},\ \tau = \frac{\tau^*\alpha_f^*}{L^{*2}},\ (x, y, B, t_b) = \frac{(x^*, y^*, l_b^*, t_b^*)}{L^*} \\
&\boldsymbol{u} = \frac{\boldsymbol{u}^* L^*}{\alpha_f^*},\ \boldsymbol{w} = \frac{\boldsymbol{w}^* L^*}{\alpha_f^*},\ P = \frac{P^* {L^*}^2}{\rho_f^* {\alpha_f^*}^2},\ T = \frac{T^* - T_c^*}{T_h^* - T_c^*}
\end{aligned} \tag{11}$$

By considering $\nabla = \nabla^* L^*$, the dimensionless equations representing the thermal and hydrodynamic behaviour of the fluid are listed below:

*Mass conservation*:

$$\nabla \cdot \boldsymbol{u} = 0 \tag{12}$$

*Momentum conservation*:

$$\frac{\partial \boldsymbol{u}}{\partial \tau} + (\boldsymbol{u} - \boldsymbol{w}) \cdot \nabla \boldsymbol{u} + \nabla P - Pr\nabla^2 \boldsymbol{u} - Pr\, Ra\, T\boldsymbol{j} = 0 \tag{13}$$

in which Rayleigh number $Ra$ and Prandtl number $Pr$ are, respectively:

$$Ra = \frac{g^* \beta_f^* \left(T_h^* - T_c^*\right) L^{*^3}}{\upsilon_f^* \alpha_f^*},\ Pr = \frac{\upsilon_f^*}{\alpha_f^*} \tag{14}$$

*Energy conservation for the fluid*:

$$\frac{\partial T}{\partial \tau} + (\boldsymbol{u} - \boldsymbol{w}) \cdot \nabla T - \nabla^2 T = 0 \tag{15}$$

The dimensionless governing equation for the conduction heat transfer and structural displacement of the flexible baffle are derived as:

*Energy conservation for the flexible baffle*:

$$\frac{\partial T}{\partial \tau} - \kappa \nabla^2 T = 0 \tag{16}$$

*Structural displacement of the flexible baffle*:

$$\frac{d^2 \boldsymbol{d}_s}{d\tau^2} - \rho_R E\, \nabla \boldsymbol{\sigma} - \rho_R E\, \boldsymbol{F}_v = 0 \tag{17}$$

The dimensionless parameters in the above equations are:

$$E = \frac{E_\tau^* L^{*^2}}{\rho_f^* \alpha_f^{*^2}},\ \boldsymbol{F}_v = \frac{\left(\rho_f^* - \rho_s^*\right) L^* \boldsymbol{g}}{E_\tau^*},\ \rho_R = \frac{\rho_f^*}{\rho_s^*},\ \kappa = \frac{k_s^*}{k_f^*} \tag{18}$$

Herein, the density of the fluid and solid are assumed identical ($\rho_f^* = \rho_s^*$) for convenience. Thus, $\rho_R = 1$ and $\boldsymbol{F}_v = 0$. In practice, the baffle could take non-zero body forces due to the density differences between the structure and the fluid inside the enclosure. In this case, $\boldsymbol{F}_v$ acts as a simple source term in Eq. (17). Applying the non-dimensional parameters presented in Eq. (11), the normalized form of the boundary conditions is:

$$\forall x, y \left| \begin{array}{l} y = 0, 0 \le x \le 1 \\ x = 0, 0 \le y \le 1 \end{array} \right. \Rightarrow T = 1,\ u = v = 0 \tag{19-a}$$

$$\forall x, y \left| \begin{array}{l} x = 1/2,\ 1/2 \le y \le 1 \\ y = 1/2,\ 1/2 \le x \le 1 \end{array} \right. \Rightarrow T = 0,\ u = v = 0 \tag{19-b}$$

$$\forall x,y\, |x = 1,\ 0 \le y \le 1/2 \Rightarrow \frac{\partial T}{\partial x} = 0,\ u = v = 0 \tag{19-c}$$

$$\forall x, y\, |y = 1,\ 0 \le x \le 1/2 \Rightarrow \frac{\partial T}{\partial y} = 0,\ u = v = 0 \tag{19-d}$$

Also, at the interface of the fluid and flexible baffle:

$$\left(\frac{\partial T}{\partial n}\right)_f = \kappa \left(\frac{\partial T}{\partial n}\right)_s,\ \frac{\partial \boldsymbol{d}_s}{\partial \tau} = \boldsymbol{u}, \boldsymbol{\sigma} \cdot n = -P + Pr\nabla \boldsymbol{u} \tag{19-e}$$

As an initial condition, the velocities and relative pressures are zero. The temperature field is uniform in the domain equal to 0.5. The local Nusselt number ($Nu$) is defined as follows:

$$Nu = -\left.\frac{\partial T}{\partial x}\right|_{x=0}\ or\ -\left.\frac{\partial T}{\partial y}\right|_{y=0} \tag{20}$$

The average Nusselt number, which indicates the total heat transfer rate, is:

$$\overline{Nu} = -\int_0^1 \left.\frac{\partial T}{\partial x}\right|_{x=0} dy - \int_0^1 \left.\frac{\partial T}{\partial y}\right|_{y=0} dx \tag{21}$$

Finally, the normalized form of the partial differential equation of the stream function is:

$$\nabla^2 \psi + \nabla \times \boldsymbol{u} = 0 \tag{22}$$

Since the cavity is closed, the value of stream function on the walls is the same and adopted as zero.

## 3 Numerical approach, gird examination, and validations

### 3.1 Numerical approach

The governing equations, along with the corresponding boundary conditions, are solved numerically. The motion of the flexible baffle occurs through the fluid inside the L-shaped enclosure, and hence, the mesh is allowed to move along with the displacement of the baffle. Arbitrary Lagrangian–Eulerian (ALE) method, which deals with such coupling of structure deflection and fluid flow, is used as an efficient technique. The details of this method are discussed in Donea and Huerta [40] and Zhang and Hisada [41].

The linear shape functions were utilized to discretize the pressure, temperature fields in the fluid domain. The quadratic Lagrange shape functions were used for the velocity components in the structure domain. Then, the residual equations for the velocity components as well as the pressure and temperature field in the fluid domain and the structure velocities at the structure domain were obtained using the standard Galerkin approach at each element. The residual equations were integrated numerically by Gaussian quadrature with second-order accuracy.

The velocity components of ***w***, which denotes the moving velocity of the mesh in the ALE system, are computed using the Laplace equation for free deformation of the mesh. The Laplace equation builds a boundary value smoothing PDE for the displacement of meshes. The boundary conditions for the Laplace equation are Dirichlet boundary conditions with zero values at fixed walls and the displacement values at the fluid–structure interface, i.e., the flexible fin walls. The time step was controlled using a Backward Differentiation Formula (BDF) with a free time-step scheme automatically [42]. The Newton method, with a damping factor of 0.8, was applied to iteratively solve the residual equations by a PARDISO solver [43–45]. The iterations were repeated until with a residual error of O $(10^{-6})$ is achieved. Finally, the streamline equation was independently computed by solving its Laplace equation in each time step by means of the computed velocity field.

### 3.2 Grid independence test

The domain is discretized using a grid of triangular elements. The mesh is refined near the boundaries. A grid-independency test is performed in order to select the optimal number of elements and verify thei accuracy. Therefore, meshes with various numbers of elements are tested and the corresponding results are shown in Table 1. It is clear that the results are mesh-independent when a mesh with 2542 (G5) elements is considered. A view of the utilized mesh is exhibited in Fig. 2.

### 3.3 Comparisons with others

Three different simulations are conducted to ensure the validity of the utilized solver and accuracy of the results. The first one, shown in Fig. 3, is the free convection of air in a cavity. The temperature field in the cavity is with the one obtained by Calcagni et al. [46]. The second one concerns the transient analysis and validated by comparing the local temperature at a defined point to the result of Xu et al. [47]. Xu et al. [47] considered a cavity divided by a conductive partition into two subdomains (Fig. 4), and the local temperature was extracted at a defined point with coordinates (− 0.0083, 0.375). Figure 4 shows that a good agreement between the temperature obtained at the defined point using the present solver and the outcomes of Xu et al. [47]. The final validation is done by comparing the deformation of the flexible wall of an enclosure to the result obtained by Kuttler and Wall [48]. As illustrated in Fig. 5, the ability of the used solver to simulate the deformation of a flexible wall is confirmed.

**Table 1** $\overline{Nu}$ and $\sigma_{max}$ at $\tau = 1$, $Ra = 10^6$, $E = 10^9$, and $B = 0.175$ considering various sizes of utilized meshes

| Grid size | Number of elements | $\overline{Nu}$ | $\sigma_{max}$ |
|---|---|---|---|
| G1 | 563 | 14.276 | 8.33E+07 |
| G2 | 742 | 14.356 | 8.93E+07 |
| G3 | 1200 | 14.842 | 9.12E+07 |
| G4 | 1559 | 14.848 | 9.86E+07 |
| G5 | 2542 | 14.856 | 9.90E+07 |
| G6 | 6670 | 14.857 | 9.90E+07 |

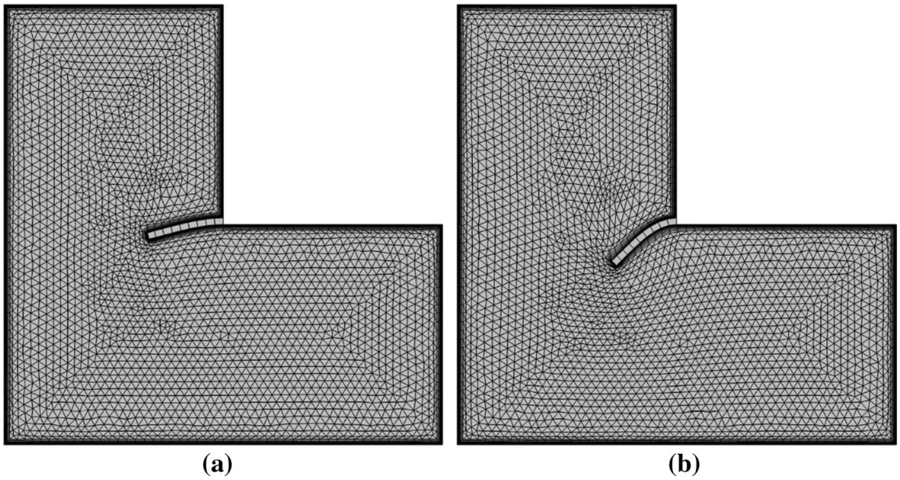

**Fig. 2** A view of the adopted mesh for the case of G5 = 2542 at **a** $\tau$ = 0.001, and **b** $\tau$ = 1

## 4 Results and discussion

In this section, the results concerning the streamlines, isotherms, maximum von Mises stress on the flexible baffle, average Nusselt number, and dimensionless temperature are reported. The considered dimensionless parameters are adopted as the elasticity modulus ($5 \times 10^8 \leq E \leq 5 \times 10^{10}$), the length of the flexible baffle ($0.05 \leq B \leq 0.225$), and Rayleigh number ($10^3 \leq Ra \leq 10^6$). The other parameters of the study are kept fixed so that $\boldsymbol{F}_v = 0$, $t_b = 0.015$, $Pr = 6.2$, and $\rho_R = 1$. The von Mises stress was used to represent the stresses in the current work.

Figure 6 illustrates the development of the streamlines with time in the enclosure. Initially, the streamlines are developed near the hot walls at the left and top parts of the cavity above the flexible baffle, which is deflected due to the flow acting on it. Shortly after, the flow separates into four recirculation zones with different flow directions appear in the flow, one above the baffle and three in the region under it. As the direction of the recirculation above the baffle is opposed to the one beneath it, the deflection of the baffle is reduced. At $\tau$ = 0.01, the three recirculation zones under the baffle unite into one zone, and the flow in the enclosure is separated into two zones, one to the left and one to the right, and the deflection of the baffle is increased. Two vortices appear in the right recirculation zone at $\tau$ = 0.02, before separating into two recirculation zones at $\tau$ = 0.06, without affecting the baffle deflection. The two zones transition then into one recirculation zone at $\tau$ = 0.3, and the flow reaches its steady-state at $\tau$ = 0.5. In the steady-state, the flow can be separated into three recirculation zones. One on the left side of the cavity where the streamlines are more concentrated near the bottom, and two on the right side, and the flexible baffle keeps the same deformation.

Figure 7 depicts the isothermal contours in the enclosure at different instants. The isotherms for high temperatures, i.e., temperatures close to the hot wall temperature, are, for all the values of $\tau$, straight lines that start at the top wall and move vertically downwards along the left hot wall, then horizontally along the hot bottom wall and finish at the right wall. The other isotherms follow the development of the flow inside the cavity. These isotherms are, initially, at $\tau = 1 \times 10^{-3}$, similar to the high-temperature isotherms. As the flow develops, their profile gets distorted in the central part of the cavity near the flexible baffle.

When the flow is in the steady-state, the isotherms of high temperature ($\theta$ between 0.7 and 1) are lines near the hot walls, while those of low temperature ($\theta$ between 0 and 0.2) remain near the cold wall and around the deflected baffle. The isotherms of intermediate temperature ($\theta$ between 0.3 and 0.8) are distributed throughout the enclosure. They start in the left region as lines between the cold and hot wall, then turn around the flexible baffle and finish as a distorted pattern in the right part of the enclosure. It is clear then that the presence of the baffle disturbs the temperature distribution in the region around it.

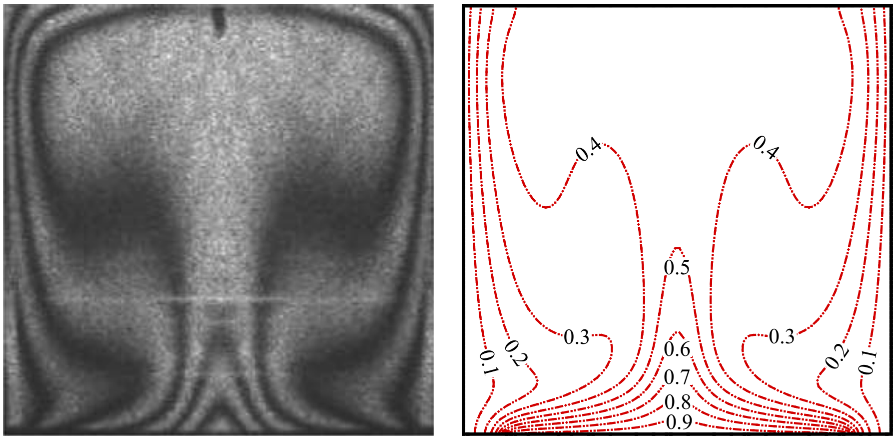

(a) (b)

**Fig. 3** **a** The isothermal contours obtained by **a** Calcagni et al. [46], **b** the ones obtained in the present study

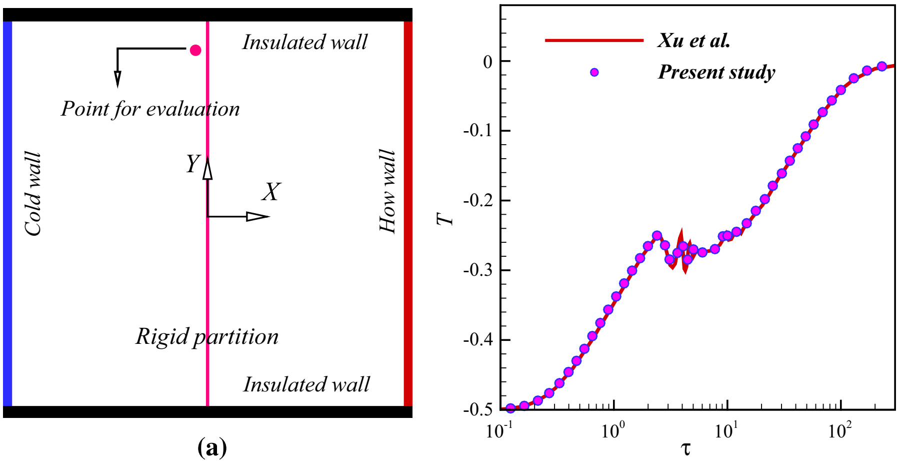

(a) (b)

**Fig. 4** Comparison of the temperature at the defined point in the enclosure obtained in the current study and the one obtained by Xu et al. [47]

The temporal evolution of the velocity surfaces inside the enclosure is plotted in Fig. 8. In the left part of the enclosure, the flow is always moving in the clockwise direction due to natural convection, as the hot fluid heated near the bottom and left walls move upwards, and the colder fluid near the right walls moves downwards. At $\tau = 6 \times 10^{-3}$, it is seen that the flow moves around the baffle, then circulates above it anti-clockwise direction. A separation zone appears where two recirculation zones with different directions are created in the right part of the enclosure.

As time goes, the velocity surfaces in the left portion of the enclosure remain unchanged, while in the right part, they transition into different patterns until finally reaching the steady-state, where the flow above the baffle is moving in the clockwise direction, while it is circulating in the opposite direction above it. A small zone in which the flow is circulating clockwise also appears to the right. These observations are in accordance with the results of Fig. 6.

### 4.1 Effect of Rayleigh number (*Ra*) on the streamlines and the isotherms

The influence of the Rayleigh number (*Ra*) on the development of the streamlines, isotherms, and velocity surfaces in the enclosure is illustrated in Fig. 9. For $Ra = 10^3$, two vortices appear in the flow in the left

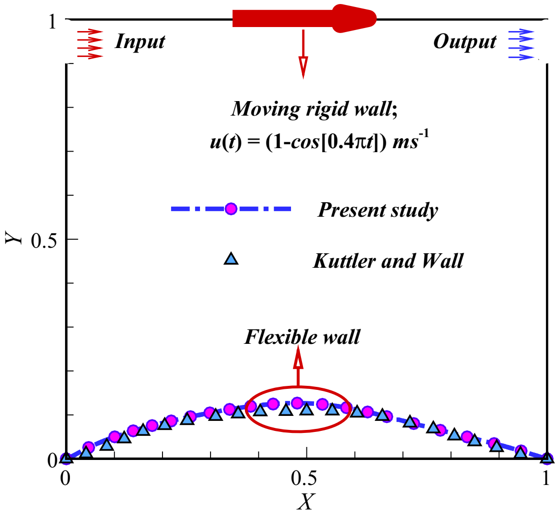

**Fig. 5** Deformation of the flexible partition in the current study and the result obtained by Kuttler and Wall [48]

region of the enclosure, while the streamlines are not fully developed in the right region under the baffle, which does not show any deflection. When *Ra* is increased to $10^4$, a circulation zone starts to appear under the baffle, which remains undeformed. The circulation zone becomes more developed as *Ra* is further increased, and finally, two circulation zones occupy the enclosure, the first in the left side of the enclosure and the second under the baffle.

A slight deflection appears in the baffle for $Ra = 10^5$, while the baffle deformation substantially increases for $Ra = 10^6$. This behaviour can be seen in the profiles of the velocity vectors. It can be particularly observed that for $Ra = 10^3$ and $Ra = 10^4$, the fluid circulates in the whole cavity in the clockwise direction with very slow flow near the right bottom wall. A zone with higher flow velocity appears above and to the left of the baffle. On the other hand, when two recirculation zones are in the enclosure for higher *Ra*, the flow circulates in the counterclockwise direction on the right side of the enclosure. High velocity is present under the baffle. The flow direction above and below the baffle is vertical going downwards, so no resistance to deflection is present in the bottom, and consequently, the deformation of the baffle becomes apparent.

The isothermal contours follow the development of the flow in the cavity. For $Ra = 10^3$ and $Ra = 10^4$, the isotherms start at the top wall and finish at the lower right wall, with some deflection around the flexible baffle. As *Ra* is increased, the isotherms patterns get distorted, notably in the central part of the enclosure below the baffle.

### 4.2 Effect of the elasticity modulus (*E*) on the streamlines and the isotherms

Figure 10 shows the effect of the elasticity modulus *E* on the streamlines, isotherms, and velocity surfaces in the cavity. It is shown that the baffle deflection increases with *E* are decreased. For $E = 5 \times 10^9$, the baffle is almost vertical, while for $E = 5 \times 10^{10}$, it remains almost horizontal. The streamlines are mainly affected in the region surrounding the baffle. A recirculation zone is always present in the left region of the enclosure for all the values of *E*.

Depending on the circulation of the fluid around the baffle, the size of the recirculation zones on the right side of the enclosure, below the baffle, changes. It can be seen that the direction of the velocity vectors varies following the flexible baffle orientation, and affects the flow patterns and velocity distribution in the bottom region of the enclosure. When the baffle is almost vertical for $E = 5 \times 10^9$, the velocity vectors surrounding it are vertical until reaching the bottom where they rotate in two recirculation zones due to convective effects. On the other hand, when the baffle is horizontal, the vectors above it are also horizontal, and a small separation zone appears beneath it, where the velocity vectors move in a vertical direction towards the bottom before continuing in the recirculation zones.

In addition, Fig. 10 shows that the inclination of the beam affects the distribution of the isothermal contours in the enclosure, following the flow patterns in each case. However, it is shown that while increasing *E* from $5 \times 10^9$ to $5 \times 10^{10}$ has some impact on the distortion of the isotherms, it does not seem to have a substantial effect on the location of the isothermal contours.

### 4.3 Effect of the baffle length on the streamlines and the isotherms

The streamlines, isotherms, and velocity surfaces are plotted in Fig. 11 for different values of the length of the flexible baffle *B*. When the baffle is short ($B = 0.05$), two vortices are present in the left and

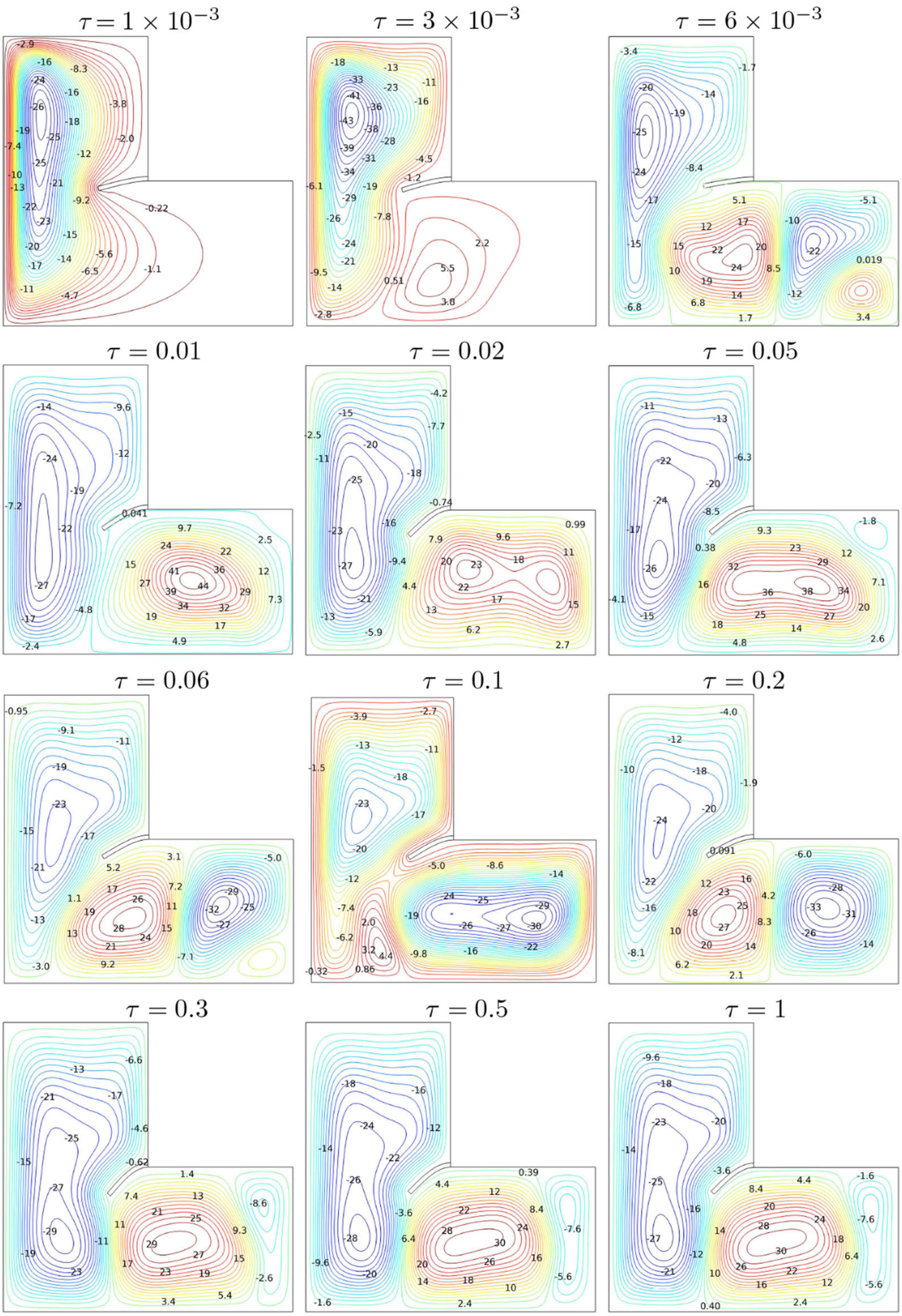

$\tau = 1 \times 10^{-3}$ $\tau = 3 \times 10^{-3}$ $\tau = 6 \times 10^{-3}$

$\tau = 0.01$ $\tau = 0.02$ $\tau = 0.05$

$\tau = 0.06$ $\tau = 0.1$ $\tau = 0.2$

$\tau = 0.3$ $\tau = 0.5$ $\tau = 1$

**Fig. 6** Time history of streamlines at $Ra = 10^6$, $E = 10^9$ and $B = 0.175$

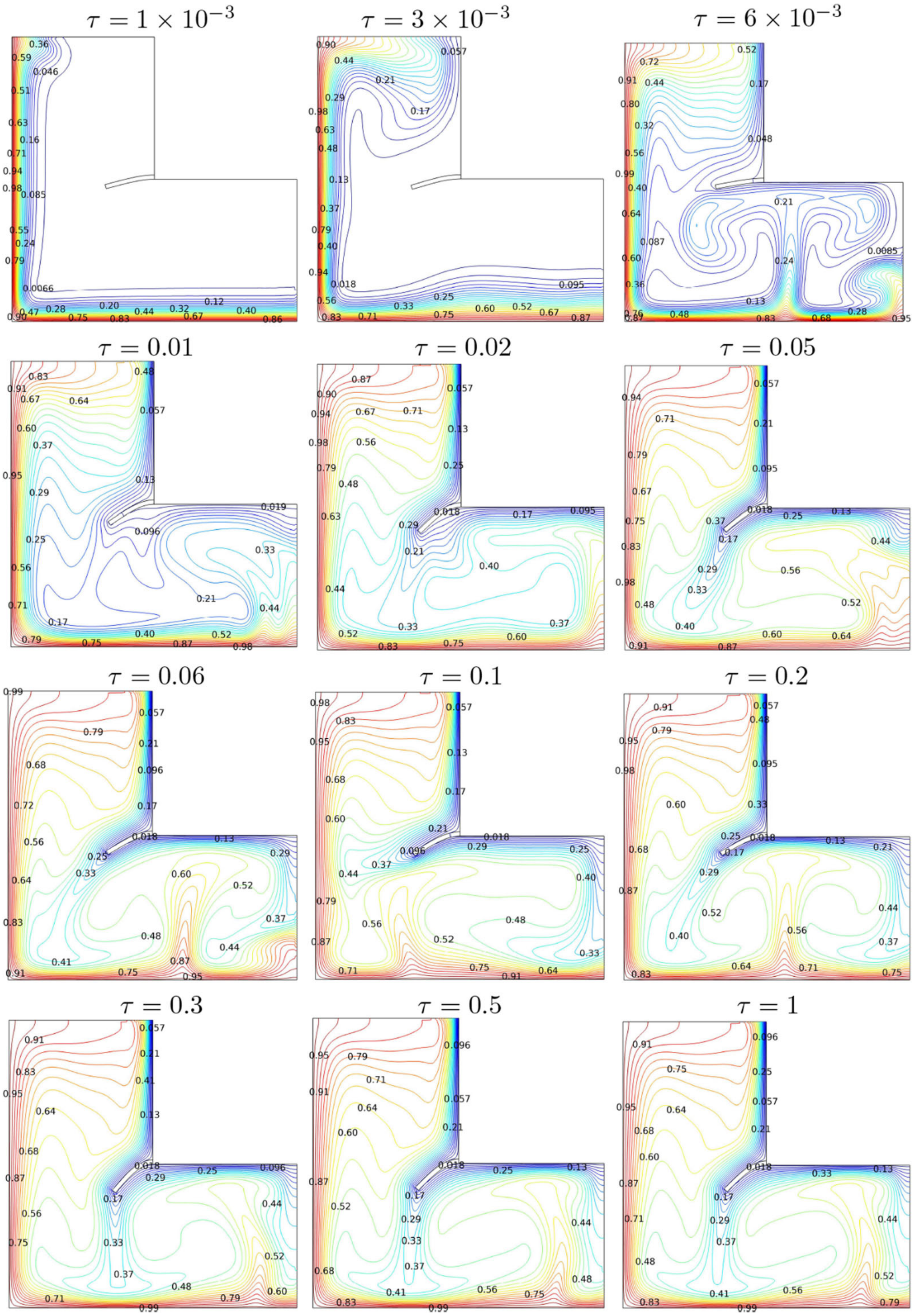

**Fig. 7** Time history of isotherms at $Ra = 10^6$, $E = 10^9$ and $B = 0.175$

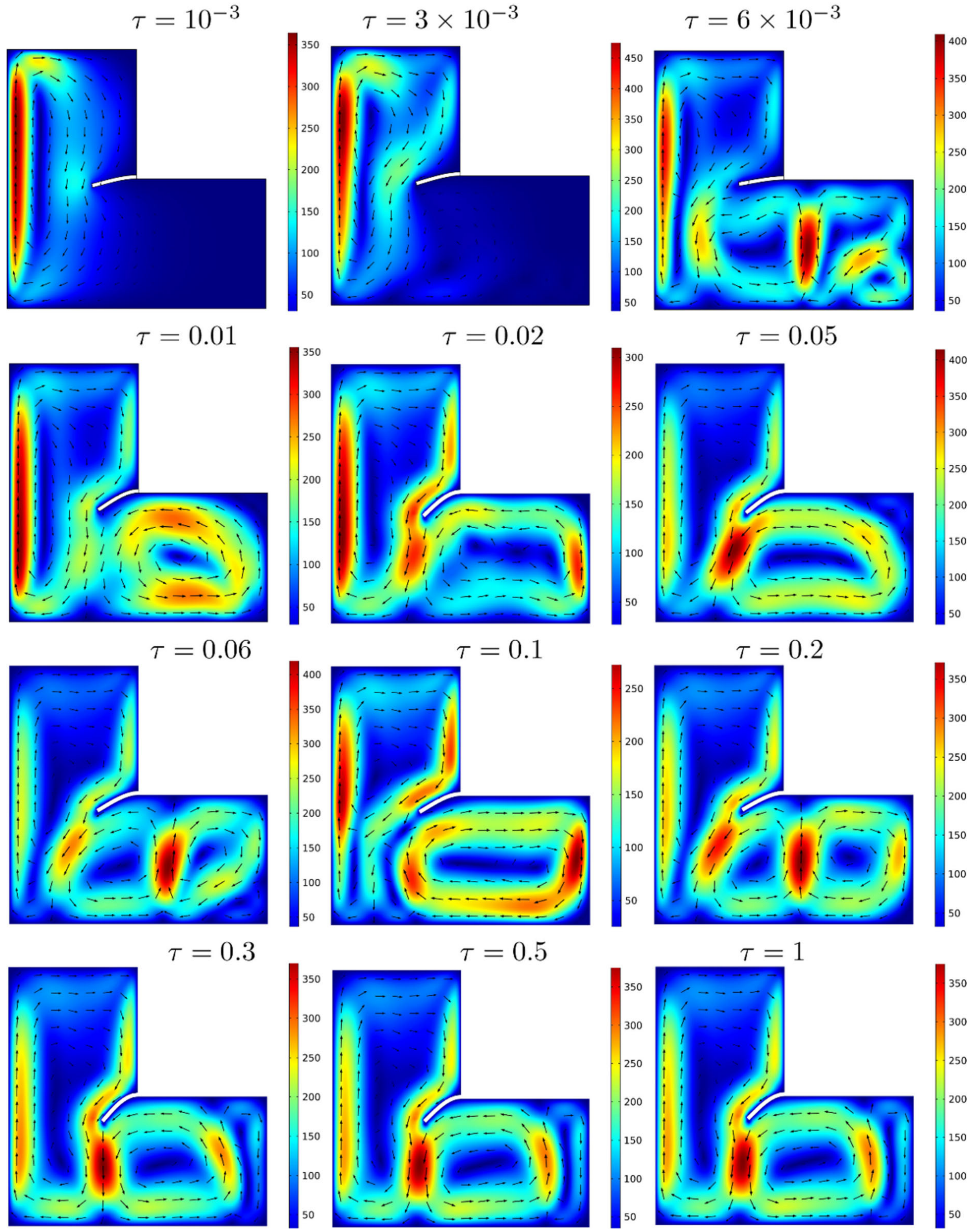

**Fig. 8** Time history of velocity surfaces at $Ra = 10^6$, $E = 10^9$ and $B = 0.175$

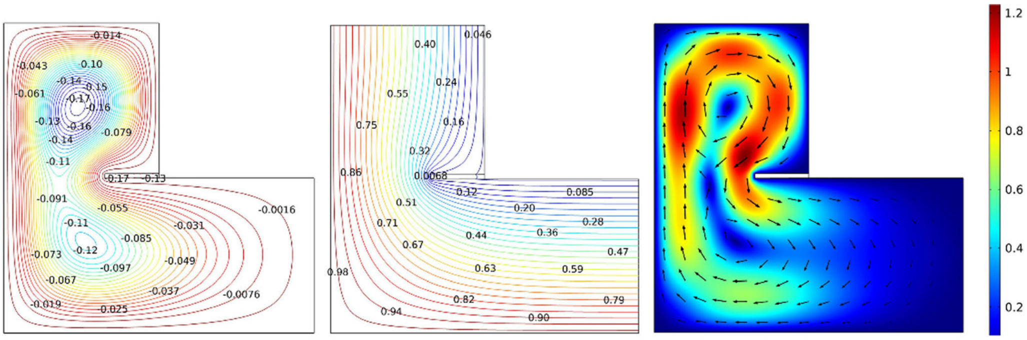

**(a)** $Ra = 10^3$

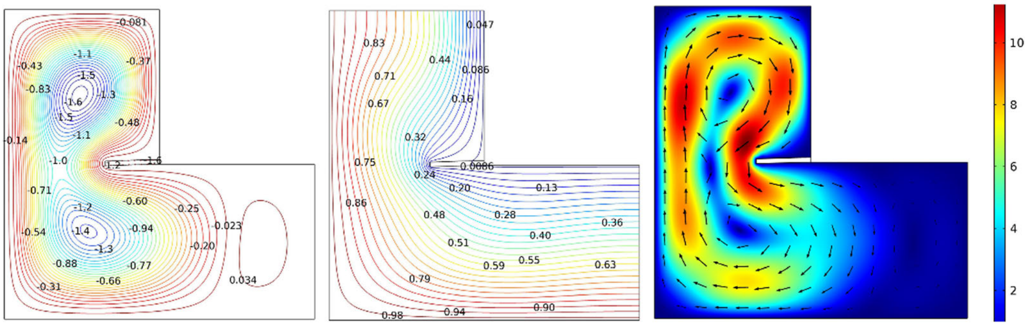

**(b)** $Ra = 10^4$

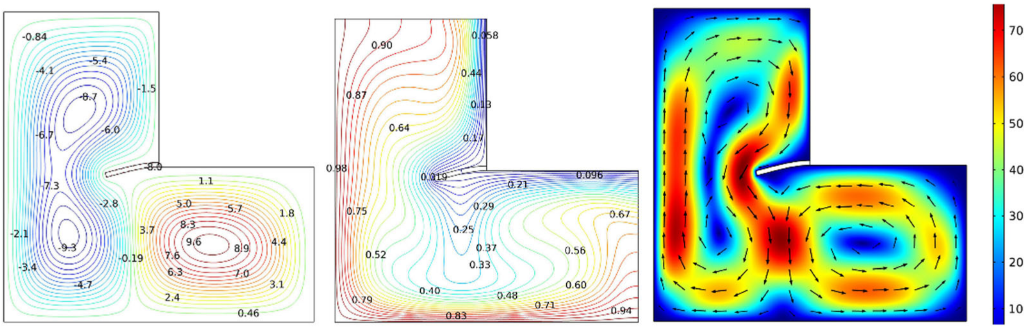

**(c)** $Ra = 10^5$

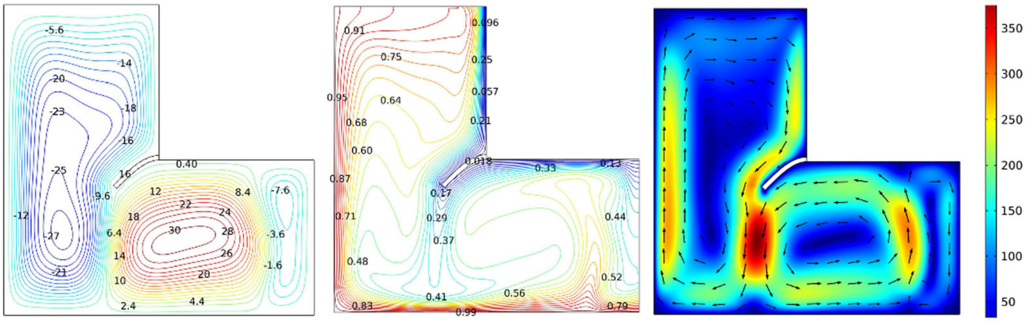

**(d)** $Ra = 10^6$

**Fig. 9** The trend of changes in the streamlines (left), temperature distribution (middle), and velocity surfaces (right) for various Rayleigh numbers at $E = 10^9$ and $B = 0.175$

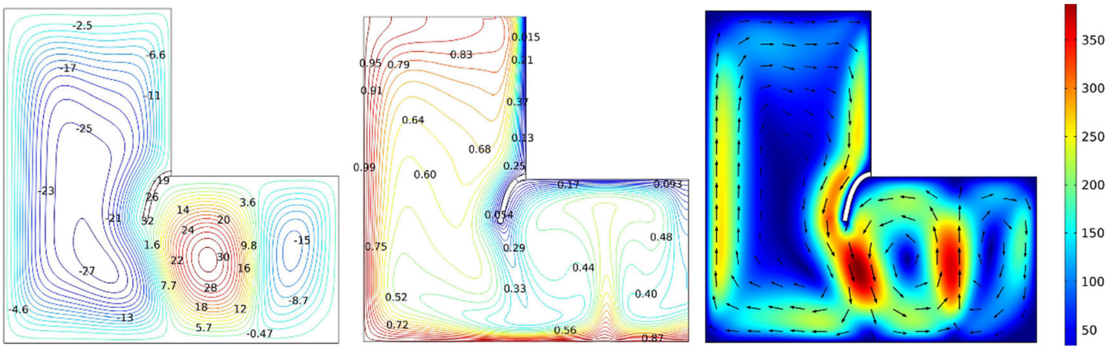

**(a)** $E = 5 \times 10^8$

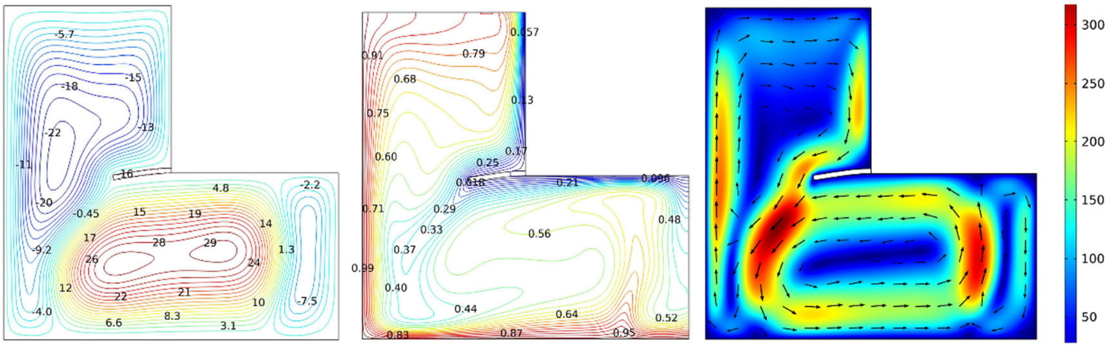

**(b)** $E = 5 \times 10^9$

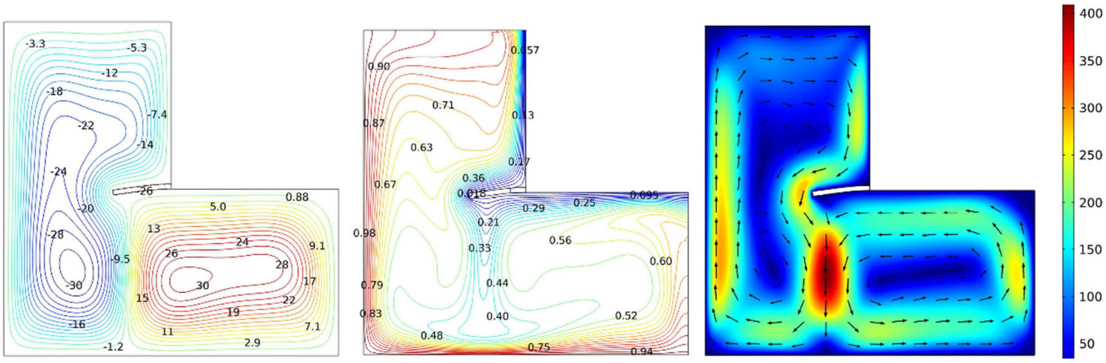

**(c)** $E = 10^{10}$

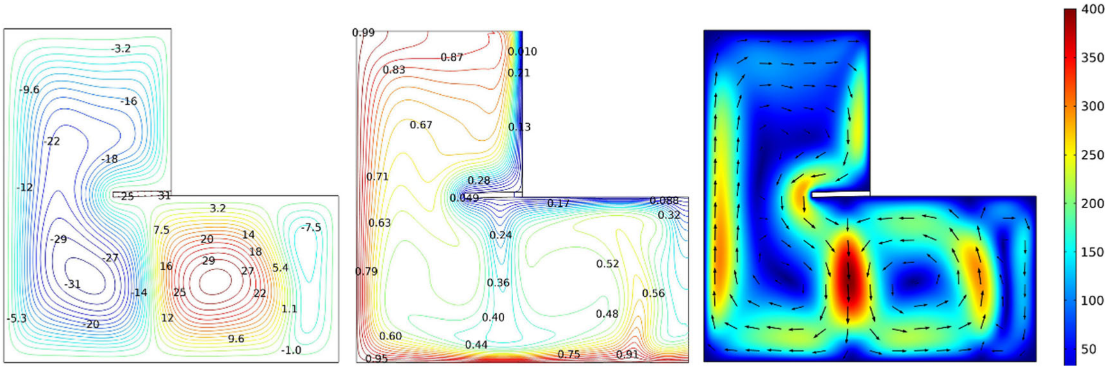

**(d)** $E = 5 \times 10^{10}$

◀**Fig. 10** The trend of changes in streamlines (left), temperature distribution (middle), and velocity surfaces (right) for the variation of the elasticity modulus (*E*) when $Ra = 10^6$ and $B = 0.175$

right portions of the enclosure. As the size of the baffle is increased, the distance between the two vortices grows until the flow separates into two recirculation zones ($B = 0.15, 0.225$). This behaviour is observed in the velocity surfaces plot, where it is shown that increasing the size of the baffle affects the distribution of the velocity vectors around it and, consequently, the flow patterns. This change in the flow patterns also affects the isotherms distribution, mainly in the central region far from the wall. The size of the baffle thus plays an important role in the flow development patterns and the temperature distribution inside the cavity.

### 4.4 Effect of *Ra* on the heat transfer rate

Figure 12 shows the variation of the steady local Nusselt number *Nu* over the hot walls and the variation of the local von Mises stress interfaces over the flexible baffle for different values of *Ra*. It is shown that the effect of *Ra* on the variation of *Nu* depends on the selected location on the hot interface. For the hot left wall, *Nu* is maximum for $Ra = 10^3$ on the top near the insulated wall. At the intersection of the two hot walls ($X + Y = 1$), *Nu* is the same for all the values of *Ra*. For the longest part of the hot interfaces, *Nu* increases with the rise of *Ra*. Indeed, *Ra* indicates the importance of free convection driving forces. Increasing *Ra* indicates that the buoyancy forces dominate the resistive viscosity, and natural convection is enhanced. In addition, it is shown that the stress over the flexible plat decreases when the value of *Ra* is reduced. The stress over the baffle is maximum for $Ra = 10^6$. Increasing the convection driving forces for higher *Ra* intensifies the fluid–structure interaction forces with the baffle, which, as a result, raises the stresses over it.

### 4.5 Effect of *E* on the heat transfer rate

The variation of *Nu* over the hot walls and the variation of the local von Mises stress interfaces over the flexible baffle are depicted in Fig. 13 for various values of *E*. The general trend of the variation of *Nu* remains the same as for all of the studied values of *E*, as the one discussed in Fig. 13 for $Ra = 10^6$. However, no clear relationship can be obtained between the variation of *Nu* and the value of *E*. For instance, over the left hot wall, *Nu* is maximum for $E = 5 \times 10^9$, while for the bottom wall, *Nu* presents a local maximum at different points, depending on the value of *E*. These observations are related to the observations discussed in Fig. 10, as varying *E*, affects the streamline patterns and flow velocity distribution above and below the baffle, and the impact of natural convection changes locally as a result. The stress over the baffle shows the same trend of variation for all the values of *E*. Nonetheless, it increases when a higher value of *E* is used, and maximum stress is obtained for $E = 5 \times 10^{10}$. Indeed, as a stiffer baffle, i.e., with a higher elastic modulus, is more resistant to the flow and deformation. This resistance results in higher stress over the baffle and smaller deflection.

### 4.6 Effect of *B* on the heat transfer rate

Figure 14 illustrates the variation of the steady local Nusselt number, i.e. *Nu*, over the hot walls and the variation of the local von Mises stress interfaces over the flexible baffle for different values of *B*. The effect of *B* on the variation of *Nu* is similar to the effect of *E*, i.e., the effect varies locally. This is due to the variation of the patterns flow passing through the gap between the baffle and the wall, with respect to the baffle size, as discussed in Fig. 11. The extent of free convection varies subsequently, leading to the local variation in the value of *Nu*. Figure 14 also shows that the profile of the variation of the stress over the baffle is the same for the various values of *B*. Nonetheless, the maximum stress increases when a larger baffle is used.

### 4.7 Variation of the maximum stress in the baffle with the various parameters

To better illustrate the effect of *E* on the heat transfer in the enclosure and on the stress over the flexible baffle, the variations of the average Nusselt number, i.e. $\overline{Nu}$, and the maximum stress on the baffle $\sigma_{max}$ as functions of *Ra* are plotted in Fig. 15 for the explored values of *E*. First, it is shown that increasing *Ra* and/or

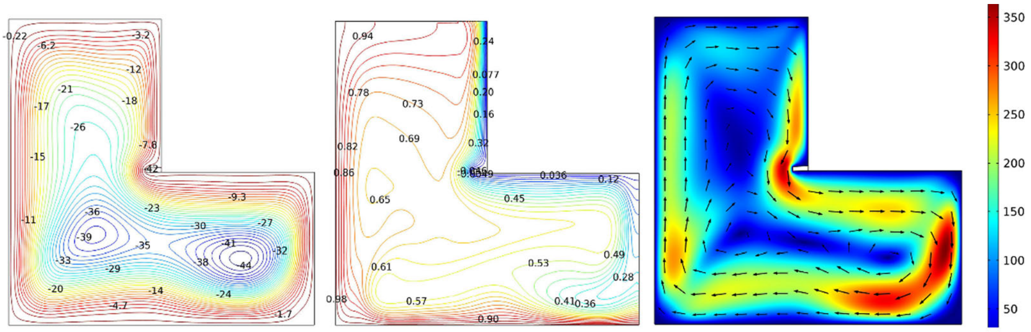

**(a)** $B = 0.05$

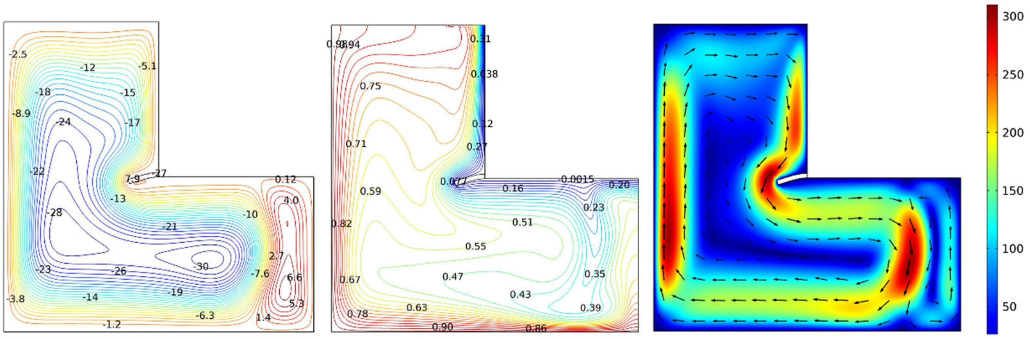

**(b)** $B = 0.1$

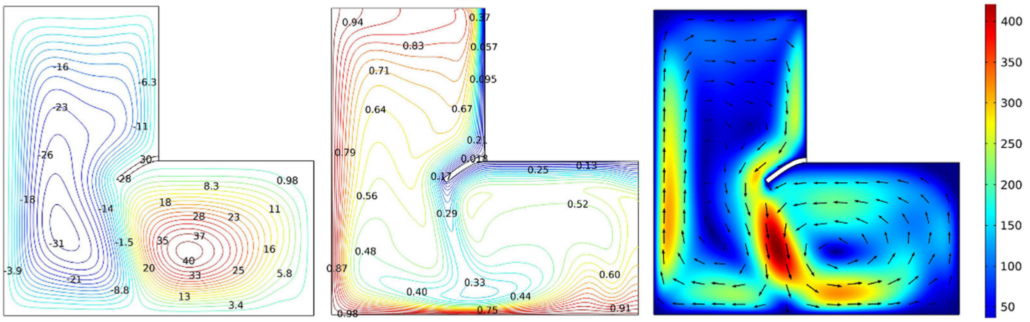

**(c)** $B = 0.15$

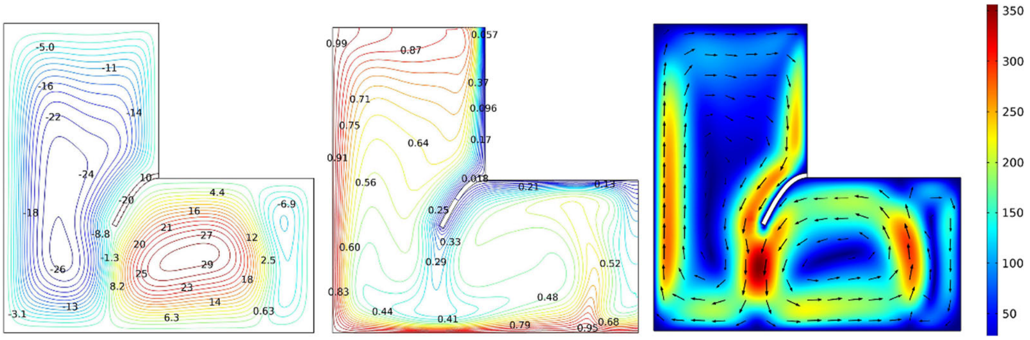

**(d)** $B = 0.225$

**Fig. 11** Variation of streamlines (left), isotherms (middle), and velocity surfaces (right) for various length of the flexible baffle ($B$) at $Ra = 10^6$ and $E = 10^9$

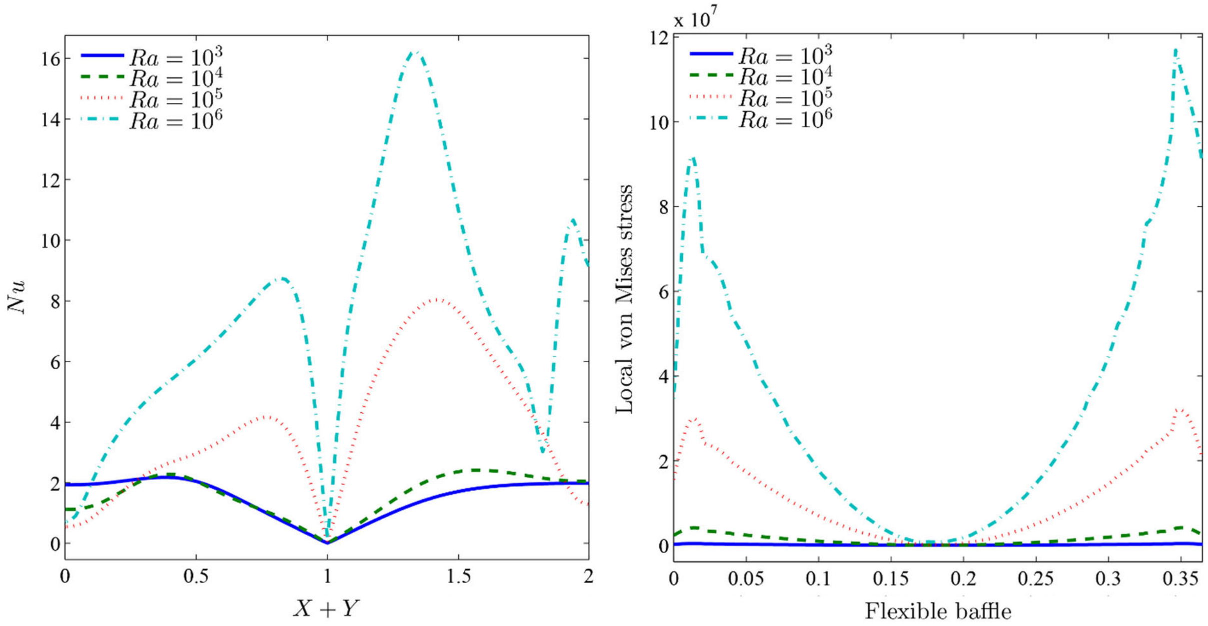

**(a)** **(b)**

**Fig. 12** Variation of the steady **a** local Nusselt number interfaces with heated walls, **b** local von Mises stress interfaces with flexible baffle for various $Ra$ at $E = 10^9$ and $B = 0.175$

$\sigma_{max}$ raises the value of $\overline{Nu}$. In addition, it can be seen that increasing $E$ does not affect the values of $\overline{Nu}$ and $\sigma_{max}$ for low values of $Ra$, typically less than $10^5$. For higher values of $Ra$, using a lower value of $E$ tends to increase $\overline{Nu}$, slightly. On the other hand, $\sigma_{max}$ substantially decreases when $E$ is reduced. Indeed, a baffle with higher $E$ shows more resistance to the flow and inhibits; consequently, the convective effects. This increased resistance leads to higher stresses in the baffle.

The effect of $B$ on the average Nusselt number ($\overline{Nu}$) and $\sigma_{max}$ as functions of $Ra$ is shown in Fig. 16. For low $Ra$, increasing $B$ tends to raise $\overline{Nu}$ slightly, as the presence of a larger baffle disturbs the flow and leads to local recirculation zones, enhancing convective heat transfer. However, for higher $Ra$, an opposite variation trend appears, and increasing $B$ tends to reduce $\overline{Nu}$, as a larger baffle shows more resistance to the intense incoming flow and inhibits heat transfer. It is also shown that raising $B$ has little effect on the variation of $\sigma_{max}$ for low $Ra$. Nonetheless, for higher $Ra$, $\sigma_{max}$ when $\sigma_{max}$ larger baffle is used. In fact, as the size of the baffle is increased, more resistance to the flow emerges in the baffle, thus increasing the maximum stress.

The variations of the unsteady $\overline{Nu}$ and $\sigma_{max}$ as functions of time for various values of $Ra$ are illustrated in Fig. 17. At $\tau = 10^{-3}$, $\overline{Nu}$ start almost at the same point for all the values of $Ra$, and as time goes, the effect of $Ra$ on the variation of $\overline{Nu}$ becomes apparent, as the value of $\overline{Nu}$ is higher when $Ra$ is increased. The same effect remains when the steady-state is reached at $\tau = 10^{-1}$. On the other hand, the effect of $Ra$ on the variation of $\sigma_{max}$ appears early on and, throughout the transition to the steady-state, $\sigma_{max}$ increases when $Ra$ is increased.

Figure 18 depicts the variations of the unsteady $\overline{Nu}$ and $\sigma_{max}$ as functions of time for different values of $E$. The effect of $E$ on $\overline{Nu}$ appears limited for all the values of $\tau$. A slight rise in the value of $\overline{Nu}$ can be observed when $E$ is decreased. On the other side, the variation of $\sigma_{max}$ presents numerous fluctuations, and as the transitions die out, it can be seen that $\sigma_{max}$ rises when a higher value of $E$ is used. The effect of $B$ on the variations of the unsteady $\overline{Nu}$ and $\sigma_{max}$ is illustrated in Fig. 19 as functions of time. It is shown that increasing $B$ tends to raise the values of $\overline{Nu}$ and $B$ for the different values of $\tau$. In addition, the time needed to reach the

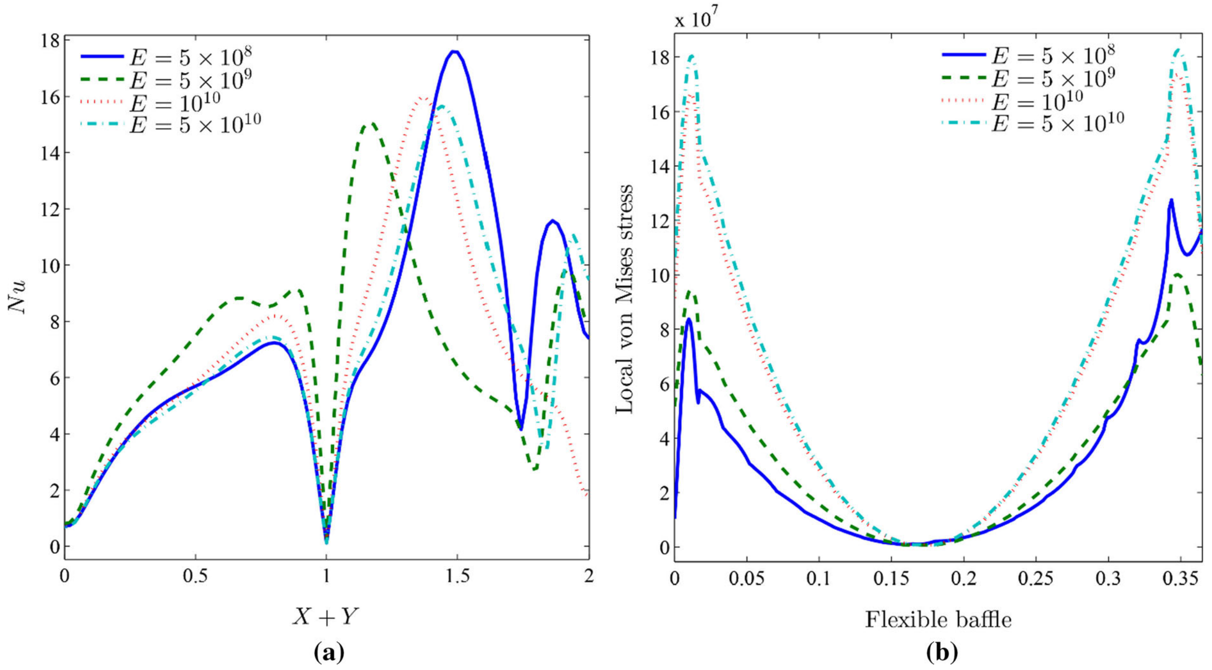

**Fig. 13** Variation of the steady **a** local Nusselt number interfaces with heated walls, **b** local von Mises stress interfaces with a flexible baffle for various $E$ at $Ra = 10^6$ and $B = 0.175$

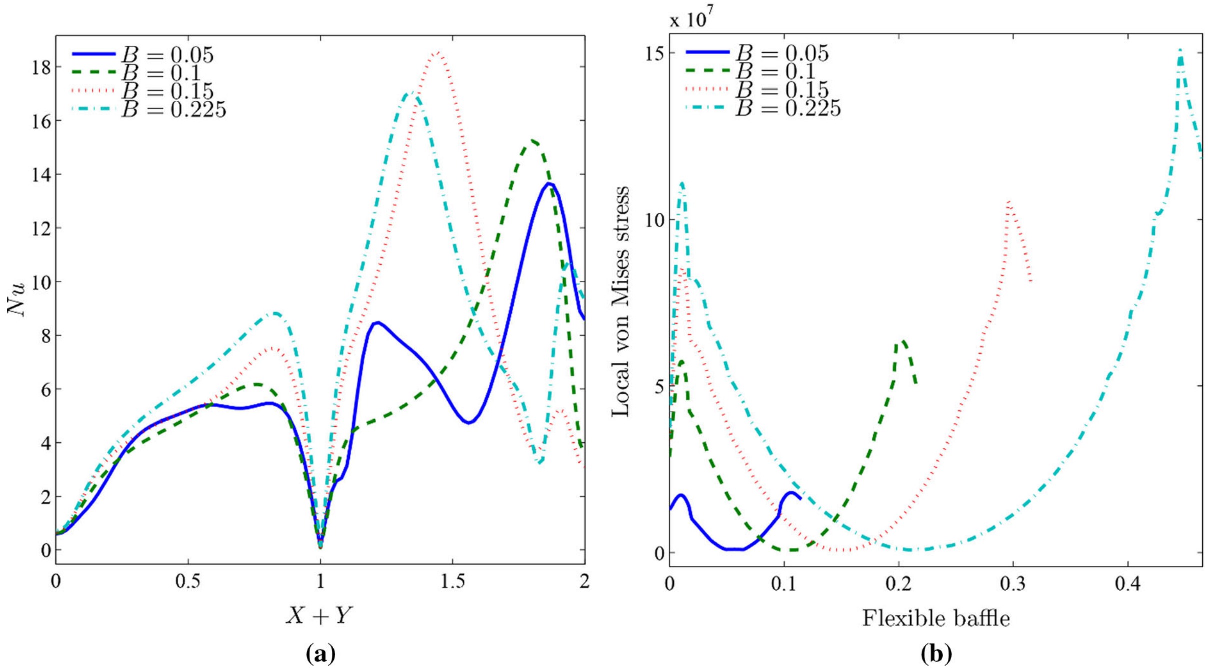

**Fig. 14** Variation of the steady **a** local Nusselt number interfaces with heated walls, **b** local von Mises stress interfaces with a flexible baffle for various $B$ at $Ra = 10^6$ and $E = 10^9$

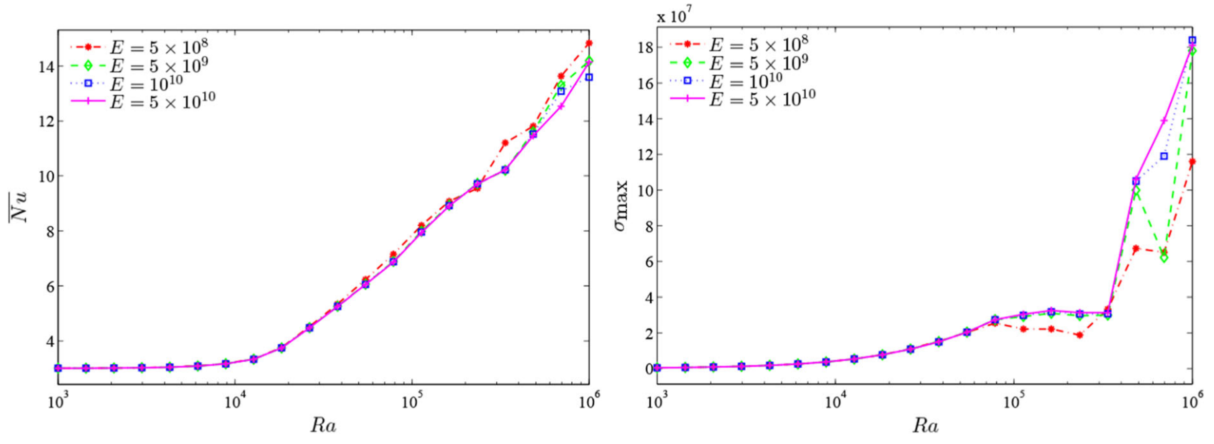

(a) (b)

**Fig. 15** Variation of the steady **a** average Nusselt number, **b** maximum von Mises stress with *Ra* for various *E* at *B* = 0.175

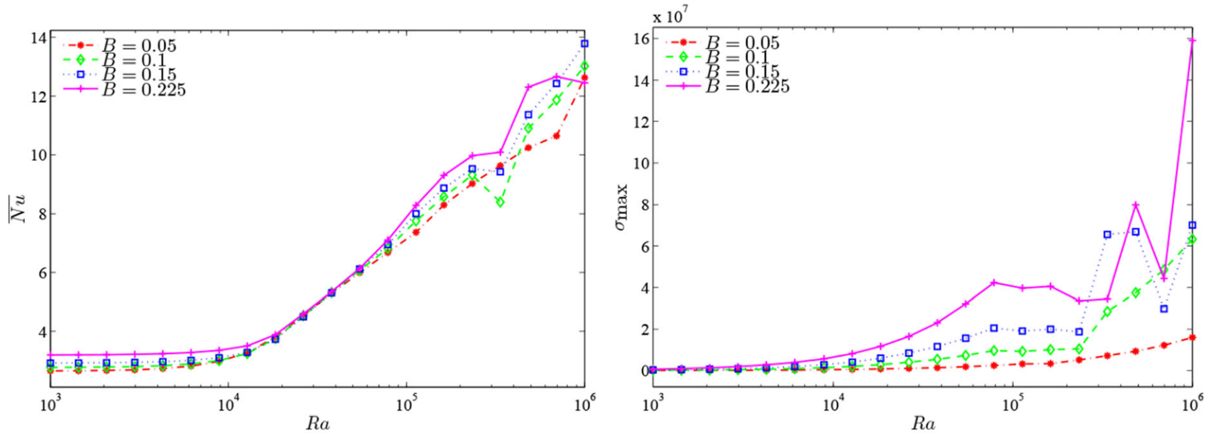

(a) (b)

**Fig. 16** Variation of the steady **a** average Nusselt number, **b** maximum von Mises stress with *Ra* for various *B* at $E = 10^9$

steady variations also varies depending on *B* in the two cases.

### 4.8 Effect of the presence of a flexible baffle

Figure 20 compares the effect of the presence of a baffle and its flexibility of the streamlines, isotherms, and velocity surfaces. Figure 21 illustrates the corresponding Nusselt numbers. The results are reported for four cases which are as follows. Case 1 shows the cavity without flexible baffle, Case 2 shows the cavity with a completely rigid solid baffle without FSI model, Case 3 depicts the cavity with flexible baffle and high elasticity ($E = 10^{11}$), and Case 4 illustrates the cavity with flexible baffle and low elasticity ($E = 5 \times 10^8$). As seen the presence of the baffle tends to suppress the natural convection flow as it acts as a barrier for flow circulation. However, as it is connected to the cold wall, it also acts as an extended surface which increases the heat transfer surface. Figure 21 shows that the presence of the baffle could eventually improve the heat transfer rate. Figure 20 indicates that a flexible baffle can bend with the fluid flow and reduce the drag forces on the fluid circulation while maintaining the extended surface for heat transfer. However, a very flexible fin can bend too much and block the flow circulation at the bottom of the cavity. As seen, the flexibility of the baffle induces a

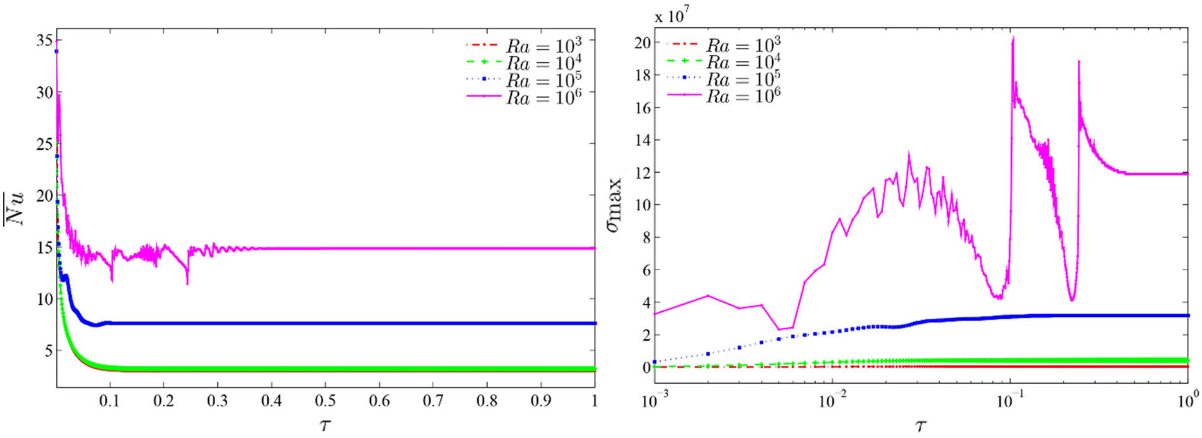

**(a)** **(b)**

**Fig. 17** Time history of **a** the average Nusselt number, **b** maximum von Mises stress with $\tau$ for various $Ra$ at $E = 10^9$ and $B = 0.175$

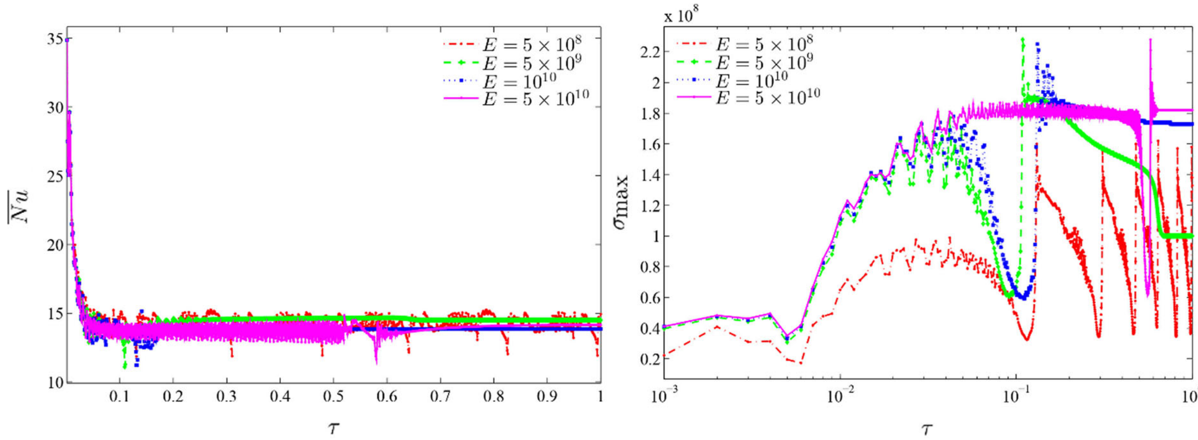

**(a)** **(b)**

**Fig. 18** Time history of **a** the average Nusselt number, **b** maximum von Mises stress with $\tau$ for various $E$ at $Ra = 10^6$ and $B = 0.175$

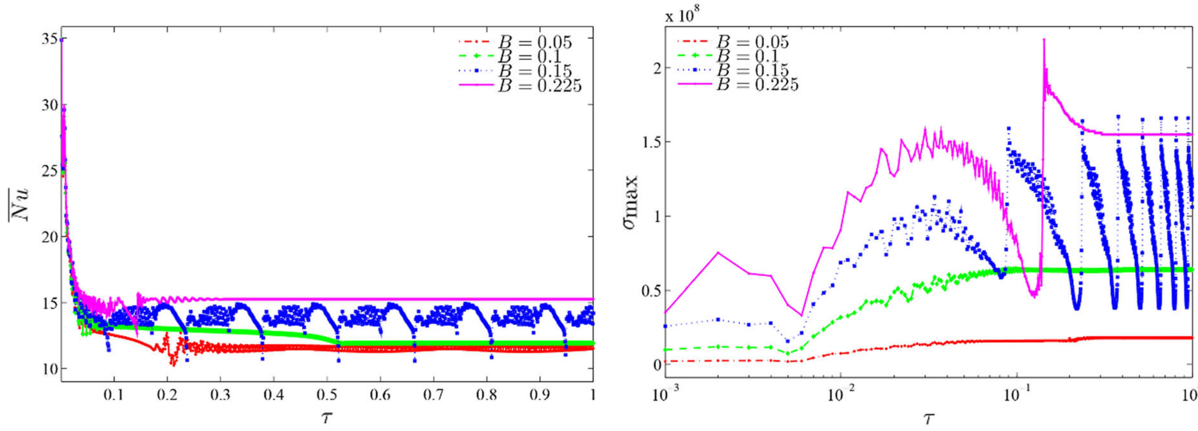

**(a)** **(b)**

**Fig. 19** Time history of **a** the average Nusselt number, **b** maximum von Mises stress with $\tau$ for various $B$ at $Ra = 10^6$ and $E = 10^9$

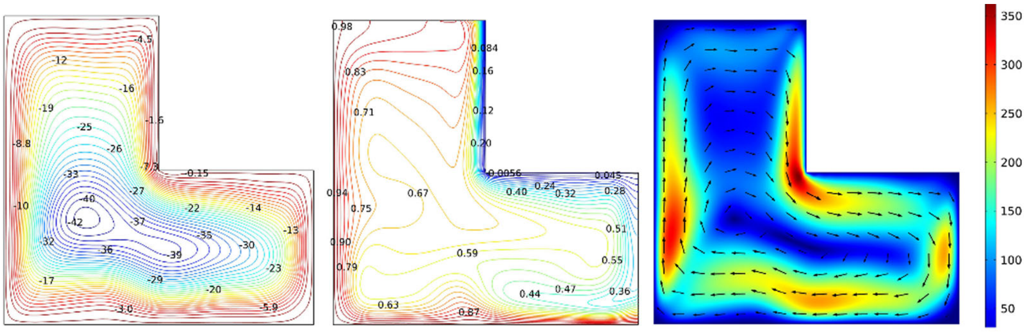

**(a)** Case 1

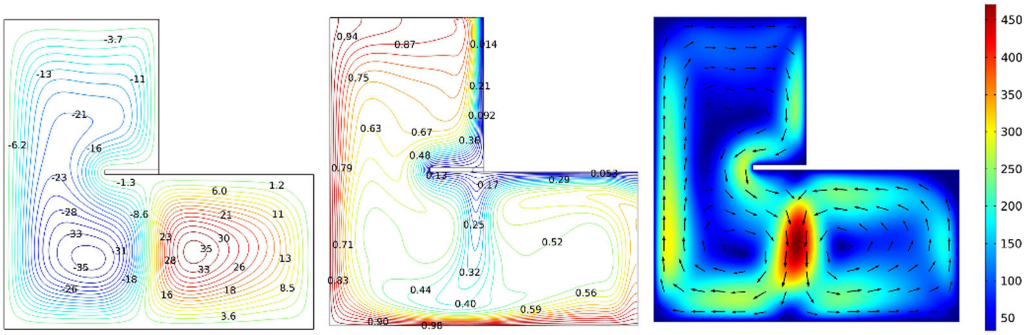

**(b)** Case 2

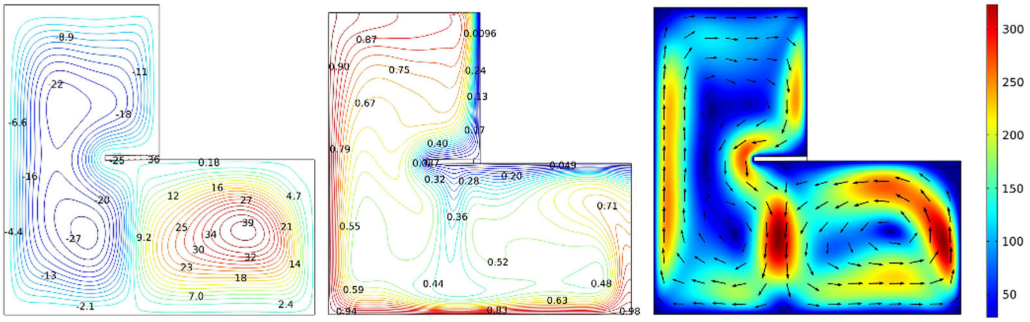

**(c)** Case 3

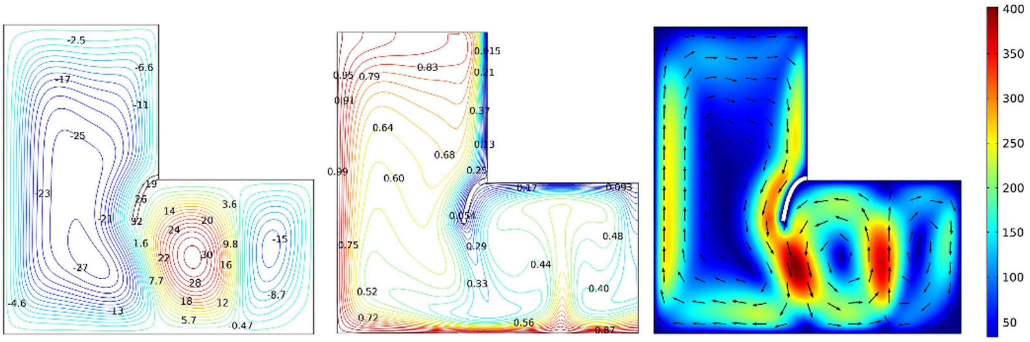

**(d)** Case 4

**Fig. 20** The effect of the presence of a baffle and its flexibility on the streamlines (left), isotherms (middle), and velocity surfaces (right) when $Ra$ = $10^6$

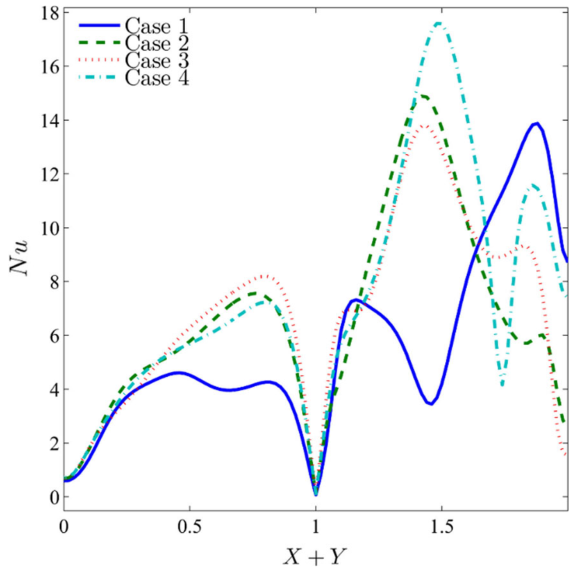

**Fig. 21** The effect of the presence of a baffle and its flexibility on the average Nusselt number

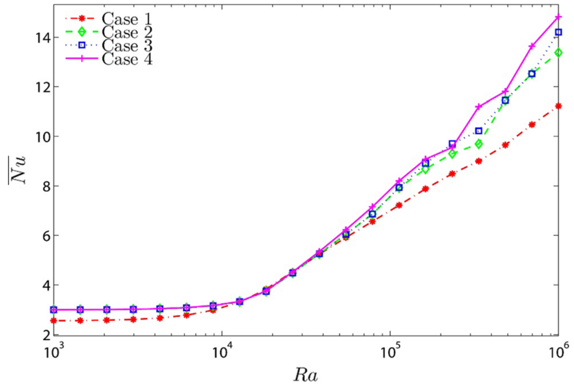

**Fig. 22** The variation of the time average Nusselt number for the investigated cases as a function of Rayleigh number

competitive situation in average Nusselt number. It improves the heat transfer in some region and deteriorates it in another region. Figure 22, depicts the average Nusselt number at various Rayleigh numbers. As seen, the case of flexible baffle provides the best heat transfer rate at high Rayleigh number values. When the Rayleigh number is large, the fluid circulation is high, which boosts the influence of the baffle shape on the hydrodynamic and heat transfer in the enclosure. Thus, it can be concluded that a baffle with moderate flexibility ($E = 5 \times 10^8$) could provide a reasonably high average Nusselt number on all areas of the heated surfaces of the cavity.

## 5 Conclusion

The free convection flow and heat transfer in a baffled L-shape enclosure were theoretically addressed using ALE associated with the moving mesh method. The finite element method was employed to solve the governing equations. The grid study was performed, and validations were reported for several cases. A summary of the results reported in the current numerical study can be presented as follows:

- Increasing Rayleigh number *Ra* enhances heat transfer in the cavity and the flexible baffle deflection, due to the dominance of free convection-driven forces with respect to the resistive viscous ones.
- The elastic modulus *E* of the flexible baffle affects the flow patterns and the distribution of the isotherms in the enclosure. As a result, heat transfer is reduced when *E* is increased, as a stiffer baffle tends to resist the fluid flow and inhibits convective heat transfer. On the other hand, the deflection is reduced, and the stress over the baffle rises when E is increased.
- The length of the baffle (*B*) also affects the flow and heat transfer in the enclosure. However, its effect is less apparent for low *Ra* (less than $10^5$). When *Ra* is increased to $10^6$, a larger baffle shows more resistance to the flow and inhibits heat transfer, while, at the same time, increases the stress over the baffle.
- The effects of *E* and *B* on flow and heat transfer are present throughout the time of the transition from unsteady to steady-state. Nonetheless, the time required to reach the steady-state varies depending on the value of *E* and/or *B*.

**Acknowledgements** The authors are grateful to the financial support received from the Malaysian Ministry of Education research Grant FRGS/1/2019/STG06/UKM/01/2.

**Compliance with ethical standards**

**Conflict of interest** The authors declare that they have no conflict of interest.

## References

1. Shi X, Khodadadi J (2005) Periodic state of fluid flow and heat transfer in a lid-driven cavity due to an oscillating thin fin. Int J Heat Mass Transf 48(25–26):5323–5337
2. Shi X, Khodadadi J (2004) Fluid flow and heat transfer in a lid-driven cavity due to an oscillating thin fin: transient behavior. J Heat Transf 126(6):924–930
3. Jamesahar E, Ghalambaz M, Chamkha AJ (2016) Fluid–solid interaction in natural convection heat transfer in a square cavity with a perfectly thermal-conductive flexible diagonal partition. Int J Heat Mass Transf 100:303–319
4. Gomes JP, Lienhart H (2013) Fluid–structure interaction-induced oscillation of flexible structures in laminar and turbulent flows. J Fluid Mech 715:537–572
5. Al-Amiri A, Khanafer K (2011) Fluid–structure interaction analysis of mixed convection heat transfer in a lid-driven cavity with a flexible bottom wall. Int J Heat Mass Transf 54(17–18):3826–3836
6. Soti AK, Bhardwaj R, Sheridan J (2015) Flow-induced deformation of a flexible thin structure as manifestation of heat transfer enhancement. Int J Heat Mass Transf 84:1070–1081
7. Sabbar WA, Ismael MA, Almudhaffar M (2018) Fluid-structure interaction of mixed convection in a cavity-channel assembly of flexible wall. Int J Mech Sci 149:73–83
8. Joshi RU, Soti AK, Bhardwaj R (2015) Numerical study of heat transfer enhancement by deformable twin plates in laminar heated channel flow. Comput Thermal Sci Int J 7:5–6
9. Park SG, Chang CB, Kim B, Sung HJ (2017) Simulation of fluid-flexible body interaction with heat transfer. Int J Heat Mass Transf 110:20–33
10. Alsabery A, Sheremet M, Ghalambaz M, Chamkha A, Hashim I (2018) Fluid–structure interaction in natural convection heat transfer in an oblique cavity with a flexible oscillating fin and partial heating. Appl Thermal Eng 145:80–97
11. Alsabery A, Selimefendigil F, Hashim I, Chamkha A, Ghalambaz M (2019) Fluid-structure interaction analysis of entropy generation and mixed convection inside a cavity with flexible right wall and heated rotating cylinder. Int J Heat Mass Transf 140:331–345
12. Mehryan S, Chamkha A, Ismael M, Ghalambaz M (2017) Fluid–structure interaction analysis of free convection in an inclined square cavity partitioned by a flexible impermeable membrane with sinusoidal temperature heating. Meccanica 52(11–12):2685–2703
13. Chamkha AJ, Miroshnichenko IV, Sheremet MA (2018) Unsteady conjugate natural convective heat transfer and entropy generation in a porous semicircular cavity. J Heat Transf 140(6):062501
14. Chamkha AJ, Miroshnichenko IV, Sheremet MA (2017) Numerical analysis of unsteady conjugate natural convection of hybrid water-based nanofluid in a semicircular cavity. J Thermal Sci Eng Appl 9(4):041004
15. Tayebi T, Chamkha AJ (2019) Entropy generation analysis during MHD natural convection flow of hybrid nanofluid in a square cavity containing a corrugated conducting block. Int J Numer Methods Heat Fluid Flow 30(3):1115–1136
16. Kumar B, Seth G, Nandkeolyar R, Chamkha A (2019) Outlining the impact of induced magnetic field and thermal radiation on magneto-convection flow of dissipative fluid. Int J Thermal Sci 146:106101
17. Dogonchi A, Armaghani T, Chamkha AJ, Ganji D (2019) Natural convection analysis in a cavity with an inclined elliptical heater subject to shape factor of nanoparticles and magnetic field. Arabian J Sci Eng 44(9):7919–7931
18. Alsabery A, Mohebbi R, Chamkha A, Hashim I (2019) Impacts of magnetic field and non-homogeneous nanofluid model on convective heat transfer and entropy generation in a cavity with heated trapezoidal body. J Therm Anal Calorim 138(2):1371–1394
19. Sardari PT, Babaei-Mahani R, Giddings D, Yasseri S, Moghimi M, Bahai H (2020) Energy recovery from domestic radiators using a compact composite metal Foam/PCM latent heat storage. J Clean Prod 257:120504
20. Shahsavar A, Goodarzi A, Mohammed HI, Shirneshan A, Talebizadehsardari P (2020) Thermal performance evaluation of non-uniform fin array in a finned double-pipe latent heat storage system. Energy 193:116800
21. Shahsavar A, Khosravi J, Mohammed HI, Talebizadehsardari P (2020) Performance evaluation of melting/solidification mechanism in a variable wave-length wavy channel double-tube latent heat storage system. J Energy Storage 27:101063
22. Mahdi JM, Mohammed HI, Hashim ET, Talebizadehsardari P, Nsofor EC (2020) Solidification enhancement with multiple PCMs, cascaded metal foam and nanoparticles in the shell-and-tube energy storage system. Appl Energy 257:113993
23. Sardari PT, Grant D, Giddings D, Walker GS, Gillott M (2019) Composite metal foam/PCM energy store design for dwelling space air heating. Energy Convers Manag 201:112151
24. Sardari PT, Giddings D, Grant D, Gillott M, Walker GS (2020) Discharge of a composite metal foam/phase change material to air heat exchanger for a domestic thermal storage unit. Renew Energy 148:987–1001
25. Arshad A, Jabbal M, Sardari PT, Bashir MA, Faraji H, Yan Y (2020) Transient simulation of finned heat sinks embedded with PCM for electronics cooling. Therm Sci Eng Prog 18:100520
26. Selimefendigil F, Öztop HF (2020) Control of natural convection in a CNT-water nanofluid filled 3D cavity by using an inner T-shaped obstacle and thermoelectric cooler. Int J Mech Sci 169:105104
27. Ahmed SY, Ali FH, Hamzah HK (2018) Heatlines visualization of natural convection in trapezoidal cavity filled with nanofluid and divided by porous medium partition. Comput Fluids. https://doi.org/10.1016/j.compfluid.2018.12.004
28. Armaghani T, Kasaeipoor A, Izadi M, Pop I (2018) MHD natural convection and entropy analysis of a nanofluid inside T-shaped baffled enclosure. Int J Numer Methods Heat Fluid Flow 28(12):2916–2941
29. Esfe MH, Arani AAA, Yan W-M, Aghaei A (2017) Natural convection in T-shaped cavities filled with water-based suspensions of COOH-functionalized multi walled carbon nanotubes. Int J Mech Sci 121:21–32
30. Morsli S, Sabeur A, El Ganaoui M (2017) Influence of aspect ratio on the natural convection and entropy

generation in rectangular cavities with wavy-wall. Energy Proc 139:29–36

31. Li Z, Barnoon P, Toghraie D, Dehkordi RB, Afrand M (2019) Mixed convection of non-Newtonian nanofluid in an H-shaped cavity with cooler and heater cylinders filled by a porous material: two phase approach. Adv Powder Technol 30(11):2666–2685
32. Miroshnichenko IV, Sheremet MA, Oztop HF, Al-Salem K (2016) MHD natural convection in a partially open trapezoidal cavity filled with a nanofluid. Int J Mech Sci 119:294–302
33. Mohebbi R, Mehryan S, Izadi M, Mahian O (2019) Natural convection of hybrid nanofluids inside a partitioned porous cavity for application in solar power plants. J Therm Anal Calorim 137(5):1719–1733
34. Selimefendigil F, Öztop HF (2019) MHD mixed convection of nanofluid in a flexible walled inclined lid-driven L-shaped cavity under the effect of internal heat generation. Phys A Stat Mech Appl 534:122144
35. Mahmoodi M (2011) Numerical simulation of free convection of a nanofluid in L-shaped cavities. Int J Therm Sci 50(9):1731–1740
36. Ma Y, Mohebbi R, Rashidi M, Yang Z (2018) Simulation of nanofluid natural convection in a U-shaped cavity equipped by a heating obstacle: effect of cavity's aspect ratio. J Taiwan Inst Chem Eng 93:263–276
37. Fard AH, Hooshmand P, Mohammaei M, Ross D (2019) Numerical study on free convection in a U-shaped CuO/water nanofluid-filled cavity with different aspect ratios using double-MRT lattice Boltzmann. Therm Sci Eng Prog 14:100373
38. Chamkha A, Ismael M, Kasaeipoor A, Armaghani T (2016) Entropy generation and natural convection of CuO-water nanofluid in C-shaped cavity under magnetic field. Entropy 18(2):50
39. Zargartalebi H, Ghalambaz M, Chamkha A, Pop I, Nezhad AS (2018) Fluid–structure interaction analysis of buoyancy-driven fluid and heat transfer through an enclosure with a flexible thin partition. Int J Numer Methods Heat Fluid Flow 28:2072–2088
40. Donea J, Huerta A (2003) Finite element methods for flow problems. Wiley, Hoboken
41. Zhang Q, Hisada T (2001) Analysis of fluid–structure interaction problems with structural buckling and large domain changes by ALE finite element method. Comput Methods Appl Mech Eng 190(48):6341–6357
42. De Los Reyes JC, González Andrade S (2012) A combined BDF-semismooth Newton approach for time-dependent Bingham flow. Numer Methods Partial Differ Equ 28(3):834–860
43. Wriggers P (2008) Nonlinear finite element methods. Springer, Berlin
44. Schenk O, Gärtner K (2004) Solving unsymmetric sparse systems of linear equations with PARDISO. Future Gener Comput Syst 20(3):475–487
45. Verbosio F, De Coninck A, Kourounis D, Schenk O (2017) Enhancing the scalability of selected inversion factorization algorithms in genomic prediction. J Comput Sci 22:99–108
46. Calcagni B, Marsili F, Paroncini M (2005) Natural convective heat transfer in square enclosures heated from below. Appl Therm Eng 25(16):2522–2531
47. Xu F, Patterson JC, Lei C (2009) Heat transfer through coupled thermal boundary layers induced by a suddenly generated temperature difference. Int J Heat Mass Transf 52(21–22):4966–4975
48. Küttler U, Wall WA (2008) Fixed-point fluid–structure interaction solvers with dynamic relaxation. Comput Mech 43(1):61–72